NASA Contractor Report 3820

5

# A Kinetic Energy Study of the Meso β-Scale Storm Environment During AVE-SESAME V (20–21 May 1979)

Matthew F. Printy and Henry E. Fuelberg

NASA

NASA Contractor Report 3820

# A Kinetic Energy Study of the Meso β-Scale Storm Environment During AVE-SESAME V (20-21 May 1979)

Matthew F. Printy and Henry E. Fuelberg

*Saint Louis University*
*Suint Louis, Missouri*

# NASA

National Aeronautics
and Space Administration

Scientific and Tschnical
Information Branch

1984

J

# ACKNOWLEDGEMENTS

TABLE OF CONTENTS

LIST OF TABLES

## LIST OF FIGURES

LIST OF FIGURES (CONTINUED)

Figure                                                                        Page

**1.** INTRODUCTION


**a.** <u>Motivation</u> **for** <u>investigatioq</u>


Atmospheric motion is characterized by sizes ranging from planetary waves down to small scale turbulent eddies. Scale interactions are observed to transfer energy both up and down this meteorological spectrum. Understanding the complex interactions between scales remains one of the most challenging topics in meteorology. Mesoscale phenomena such as severe thunderstorms are influenced by both larger and smaller scales of motion. In their developing and advanced stages, thunderstorms apparently modify the wind and thermal structure of their surrounding environments through scale interaction or "feedback" mechanisms which presently are not well understood.

Inadequate data for describing mesoscale weather phenomena have hindered research into scale interactions. The resolution of the routine upper air network is too coarse in both space and time to properly capture mesoscale weather events since observations are taken every **12** h at an average station spacing of 400 **km.** However, special mesonetworks developed for the Atmospheric Varia- bility Experiment - Severe Environmental Storms and Mesoscale Experiment (AVE–SESAME) (Alberty <u>et</u> <u>al.</u>, **7979;** Hill <u>et</u> <u>al.</u>, **1979;** Barnes, **1981)** are allowing researchers to probe, measure, and observe the mesoscale storm environment at a much finer resolution

than is routinely possible. Many investigations utilizing the special data are now underway to learn more about the complex structure of mesoscale weather phenomena and their interactions with the lower scale environment. Our ability to forecast weather events will improve. for example, as our knowledge of scale interactions increases and the findings are incorporated into the numerical prediction models.

One way to increase our understanding of thunderstorm-environment interactions is through an energy analysis of the storm's surroundings. The research described here concerns the environmental kinetic energy budget of an area of intense thunderstorms that occurred during the fifth AVE–SESAME period (20–21 May 1979). By using meso β-scale data with an average station spacing of 75 km at either 1.5 or 3 h intervals, a detailed description of variations near the storms over central Oklahoma can be obtained. The energy processes are examined prior to, during, and after peak storm activity in order to better understand energy fluctuations related to the convection.

b.  Past studies

Diagnostic studies using conventional rawinsonde data suggest that organized convective activity alters its larger scale environment. Numerical simulations by Aubert (1957) showed that latent heat release associated with convective activity produced

2

increased low level convergence and enhanced upper level divergence. In addition, height rises were found to occur in the upper troposphere, whereas height falls occurred near the surface. Using Conventional rawinsonde data and satellite imagery, Ninomiya (1971) detected a mid-tropospheric warm core, strong low level convergence. and increased upper level divergence in the storm surroundings, A mid-tropospheric jet maximum formed northwest of the convective area in response to a strong thermal gradient. As the storms developed, a low level jet intensified nearby.

More recently, Maddox (1980), Maddox **et al.** (1980), and Fritsch and Maddox (1980, 1981a,b) used enhanced, infrared satellite imagery and conventional rawinsonde data to define and describe the Mesoscale Convective Complex (MCC). MCC's are large, continuous, nearly circular areas of intense storms that last for at least 6 h. The size of the MCC cloud shield may exceed that of an individual thunderstorm by more than two orders of magnitude, They are thought to modify their larger scale environment to the extent that the evolution of future synoptic-scale systems **is** affected (Maddox, 1980). Environmental conditions near the complexes include areas of mid-tropospheric warming and ascent, enhanced low level convergence and upper level divergence, regions of upper level ridging and anticyclonic flow, and the formation of jet maxima on their poleward sides. Numerical simulations by Fritsch and Maddox (1981b) have duplicated some of the larger scale environmental modifications associated with areas of convec-

tive activity.

In addition to the synoptic-scale studies, mesoscale investigations of storm-environment interactions include those by Fankhauser (1969, 1971, 1974), Sanders and Paine (1975), Ogura and Chen (1977), Sanders and Emanuel (1977), Ogura and Liou (1980), Moore and Fuelberg (1981), Vincent et al. (1981), Anthes et al. (1982), Park and Sikdar (1982), and Vincent and Carney (1982). These diagnostic studies have confirmed the findings that were observed at the synoptic scale. Although, it is believed that the thunderstorms produced many of the observed environmental variations, more detailed investigations are needed to understand the mechanisms involved.

The literature contains relatively few studies describing the energetics of the convective storm environment. Most previous diagnostic kinetic energy investigations have focused on synoptic-scale systems such as extratropical cyclones. Those studies that have considered the energetics of the convective environment suggest that large areas of storms modify the surrounding synoptic-scale energy balance. Vincent and Schlatter (1979) proposed that deep cumulus convection could supply kinetic energy to the synoptic-scale flow. In their study involving the remains of tropical storm Candy, areas of kinetic energy increase and positive dissipation agreed closely with locations of the convection. Robertson and Smith (1980) investigated the energetics of two extratropical cyclones that produced the Jumbo (3-4 April

4

1974) and Palm Sunday (10-11 April 1965) tornado outbreaks. Using synoptic-scale rawinsonde observations every 12 h, they found major energy activity associated with the cyclones that produced the outbreaks.

With the completion of the Atmospheric Variability Experiments (AVE) and the AVE-SESAME projects, studies incorporating higher resolution data now are being reported. Fuelberg and Scoggins (1978) used AVE IV rawinsonde data having a synoptic-scale spacing but a subsynoptic-scale time interval to compute the kinetic energy balance of the Mesoscale Convective Complex described by Maddox et al. (1980). Rather tranquil conditions existed for the analysis region as a whole, whereas very active energy processes occurred within the areas of convection. The storm environments were characterized by generation of kinetic energy by cross-contour flow, horizontal flux divergence near jet stream level, upward transport by large scale ascending motion, and transfer of energy from resolvable to non-resolvable scales of motion (negative dissipation). They also noted that maximum energy conversion and transport occurred near the times and locations of greatest storm activity, thereby suggesting that energy variations were due, in part at least, to the convection.

Using National Weather Service (NWS) rawinsonde observations, Fuelberg et al. (1980) examined the synoptic-scale kinetic energy balance during the deadly Red River Valley tornado outbreak which coincided with the first AVE-SESAME period (10-11 April 1979).

5

The effects of upper level jet intrusion dominated the energy budget for the entire analysis region. Horizontal flux convergence and cross-contour destruction of kinetic energy associated with supergradient flow were the major processes. In contrast, the energetics of the storm environment included generation of kinetic energy and positive dissipation. Fuelberg et al. (1980) could not isolate possible feedback mechanisms from the storms due to strong, pre-existing dynamic forcing. They hypothesized that subsynoptic-scale data would be useful for resolving storm-environment interactions in these situations.

A subsynoptic-scale kinetic energy study of the Red River Valley tornado outbreak was recently conducted by Fuelberg and Jedlovec (1982). The combination of NWS and special rawinsonde observations provided a superior resolution of smaller scale features than was obtained by Fuelberg et al. (1980). Once again, it was found that the energetics of the storm environment differed greatly from that of the overall analysis region. Magnitudes of energy processes were larger at the finer scale of resolution, and effects of the convection were more apparent.

The only kinetic energy budget studies of the meso β-scale storm environment appear to be those by McInnis and Kung (1972), Kung and Tsui (1975), and Tsui and Kung (1977) who utilized rawinsonde data from the National Severe Storms Laboratory (NSSL). With an average station spacing of 85 km and observations at 1.5 - 3 h intervals, the data provided a detailed description of energy

a

variations within the mesoscale storm environment, The convective environment was energetically active and characterized by intense generation and dissipation of kinetic energy in the upper layers of the atmosphere, On the other hand, periods without storms contained strong destruction of kinetic energy by cross-contour flow and transfer of energy from subgrid to grid scales of motion. Magnitudes of meso 8-scale energy processes varied widely depending on the presence and strength of the convective storms, but in some cases, values were an order of magnitude larger than corresponding processes on the synoptic scale.

c. **Objectives**

The objective of this research is to investigate the kinetic energy balance of a mesoscale storm environment as a way to increase our understanding of how areas of convection modify their larger scale surroundings. Special emphasis is placed on the energy balance in order to explain observed wind variations. Meso β-scale rawinsonde data from the fifth **AVE-SESAME** period are used. In contrast to mesoscale studies by Kung which emphasized a collection of days, the current investigation is a detailed analysis of a single **24** h period. Horizontal maps of energy parameters and other diagnostic results that have not been presented previously at this scale will be described.

The specific topics that are investigated include

1) descriptions of wind and kinetic energy variations within the analysis region,

2) relationships between temporal variations in the kinetic energy budget, wind variations, and the convective activity,

3) agreements between horizontal patterns of energy parameters and locations of the convection,

4) a comparison of the energetics of the same analysis region derived from different scales of resolution, and finally,

5) an error analysis on the derived energy parameters.

## 2. METHODOLOGY

### a. Theoretical development

Both synoptic-scale motions and subsynoptic-scale motions outside of convective cells are quasi-horizontal and virtually hydrostatic. Therefore, the theory used in large scale energy analyses can be extended to meso 8-scale studies by utilizing higher resolution data (Kung and Tsui, 1975). This study uses the kinetic energy budget equation for a fixed, limited volume in isobaric coordinates which is given by Ward and Smith (1976) as:

$$\frac{\partial K}{\partial t} = \iint -\vec{V}\cdot\vec{\nabla}\phi - \iint \vec{\nabla}\cdot k\vec{V} - \iint \frac{\partial \omega k}{\partial p} + \iint \vec{\nabla}\cdot\vec{F} + \int k_o \frac{\partial p_o}{\partial t} , \qquad (1)$$

(A)　　　(B)　　　(C)　　　(D)　　　(E)　　　(F)

where

$$\iint = \frac{1}{gA} \iiint dx\ dy\ dp,$$

$\vec{V}$ is the horizontal wind velocity,

$\omega$ is the vertical motion in isobaric coordinates,

$k = (u^2 + v^2)/2$ is the horizontal kinetic energy per unit mass,

$K = \iint k$,

$\phi = gz$ is geopotential height,

$\vec{F}$ is the frictional force,

A is the computational area, and

$_o$ is a subscript denoting surface values.

9

Local changes of kinetic energy , term (A) above, are due to five processes. Term (B) represents generation of kinetic energy due to cross-contour flow over geopotential height gradients. Terms (C) and (D) denote horizontal and vertical components of flux divergence, respectively. Term (F) represents variations in energy due to changes in mass of the volume being studied. Its value was found to be several orders of magnitude smaller than those of the other terms; and, therefore, it will not be considered further. Finally, term (E) conceptually represents thermodynamical and mechanical frictional processes. This term cannot be treated explicitly and is therefore computed as a residual to balance the other terms of the equation. In this way, the residual term not only represents frictional processes, but also transfers of energy between resolvable and unresolvable scales of motion, together with possible error from the calculation of the other terms. It is commonly called the dissipation term. Since the resolvable scales of motion are known, this term allows one to infer the importance of motions which are not readily detected with the input data and computational procedures being used.

b. Data

The case being studied is the fifth day (20-21 May) of AVE-SESAME 1979. Rawinsonde data were gathered from twenty sites in Oklahoma and Texas at either 1.5 or 3 h intervals, i.e., on 20 May

at **1100, 1400, 1700, 2000, 2130,** and **2300** GMT and on **21** May at **0200, 0500, 0800,** and **1100** GMT. The average station spacing was approximately **75 km** (meso β-scale) which **is** similar to that of data sets collected by the National Severe Storms Laboratory (NSSL) ■ In addition **twenty-three** National Weather Service (NWS) sites surrounding the mesonetwork also collected data every **3** h. These stations had the conventional synoptic–scale spacing of 400 **km.** Figure 1 shows the location of the meso β (storm scale) network in relation to the routine rawinsonde stations together with a detailed view of the special sites. Soundings were terminated at 100 mb, and no data were gathered for Norman, OK (OUN). Names of the special sites are given in Table **1.** Reduction procedures used to process the rawinsonde data are described by Fuelberg **(1974),** while tabulated results at **25** mb intervals are given by Sienkiewicz et al. **(1981).**

It must be emphasized that we are investigating energy fluctuations of the gtorm environment rather than individual convective cells. Although the special mesonetworks of AVE–SESAME **1979** have a much higher density than ordinary upper **air sites,** even the storm scale network **still is** too coarse to resolve details **of** particular cells, According to Sienkiewicz && (1981), only four sondes from the special network exhibited large variations in ascent rate which might indicate penetration into active convective cells. A careful time and space continuity check of the four soundings, however, suggested that they also were representative

11
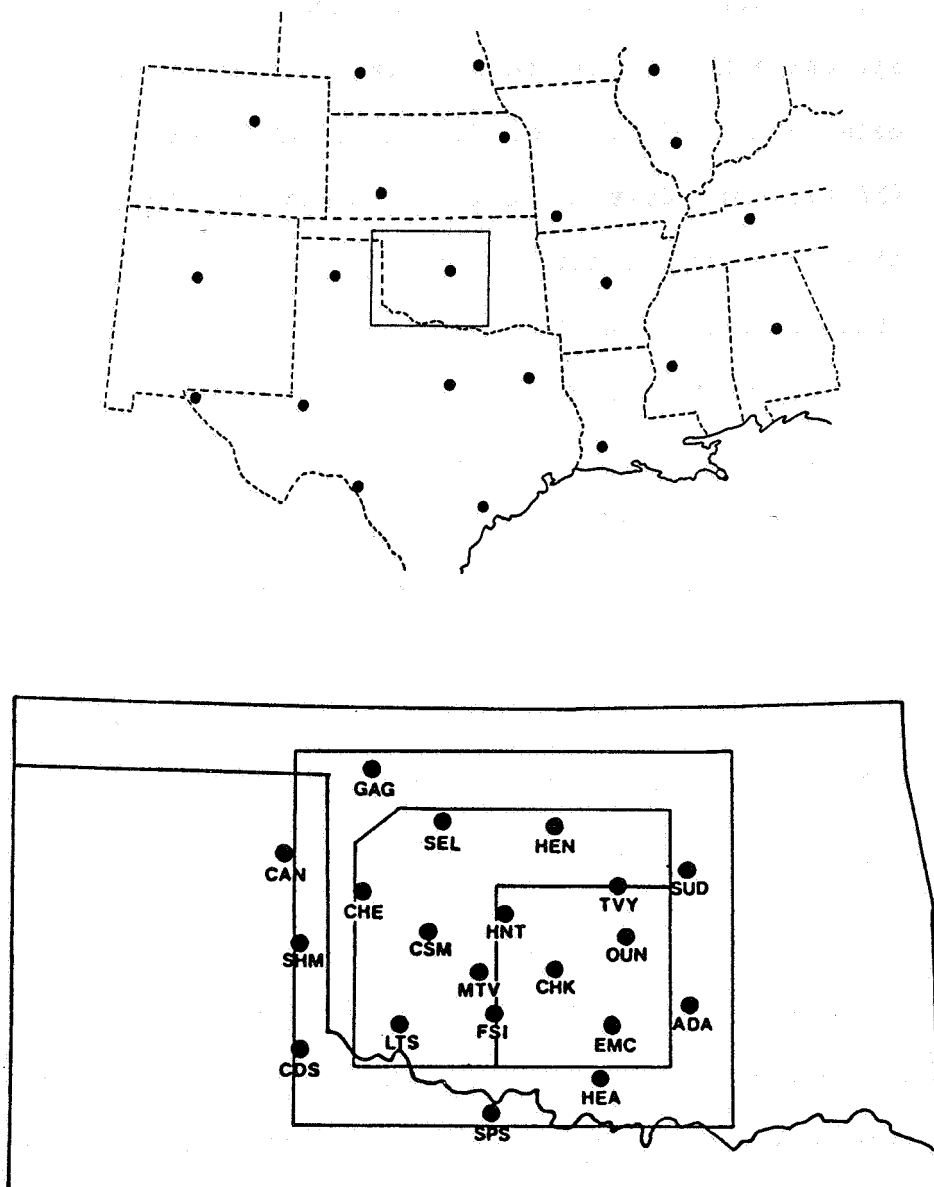
Fig. 1.  Rawinsonde networks participating in AVE-SESAME V.  The
top diagram shows the synoptic-scale network while the
bottom gives the meso β-scale network.  The storm scale
domain is superimposed on the large scale domain in the
top figure.  Outlines (bottom) indicate the 15 X 13
analysis region (outer),  the overall energy averaging
region (middle),  and the subvolume encompassing the
upper level wind couplet (inner).

Table **1.** Names of the special storm scale radiosonde
stations participating in AVE–SESAME 1979.

| | |
|---|---|
| ADA | Ada, OK |
| LTS | Altus, OK |
| CAN | Canadian, TX |
| CHE | Cheyenne, OK |
| CHK | Chickasha, OK |
| CDS | Childress, TX |
| CSM | Clinton Sherman, OK |
| EMC | Elmore City, OK |
| FSI | Ft. Sill, OK |
| GAG | Gage, OK |
| HEA | Healdton, OK |
| HEN | Hennessey, OK |
| HNT | Hinton, OK |
| **TVY** | K T W, OK |
| **MTV** | Mountain View, OK |
| **OUN** | Norman, OK |
| SEL | Seiling, OK |
| **SHM** | Shamrock, TX |
| **SUD** | Stroud, OK |
| **SPS** | Wichita Falls, TX |

of the storm environment, i.e., no unusual characteristics were noted. Moreover, the objective analysis procedures described next should greatly filter any non-environmental effects that escaped detection. Thus, data from the four soundings could be used in the later computations.

As an aid in the diagnostic study, radar summary data from the National Meteorological Center (NMC) and GOES satellite imagery obtained from NASA's Marshall Space Flight Center (MSFC) also were utilized.

## c. Data handling procedures

The use of subsynoptic-scale data, may violate several assumptions that normally are made as part of large scale data handling procedures. Furthermore, since subsynoptic-scale resolution depends on having as much data as possible, it is desirable to generate values for missing soundings when feasible. Consequently, several modifications were made to the usual synoptic-scale techniques.

Rawinsonde data collected during AVE-SESAME V were generally found to be of good quality. Nevertheless, several problems remained in the final tabulated product. First, data from ten storm scale soundings appeared questionable because their values did not show reasonable time and space continuity (Table 2). Therefore. these soundings were removed from the data set.

Table 2.  Mesonetwork soundings removed from the
          data base because of abnormal characteristics.

| Station | Date/Time |
|---|---|
| Cheyenne, OK | 20 May/1100 GMT |
| | 20 May/1400 GMT |
| | 20 May/1700 GMT |
| | 20 May/2000 GMT |
| | 20 May/2130 GMT |
| | 20 May/2300 GMT |
| | 21 May/0800 GMT |
| Seiling, OK | 20 May/1700 GMT |
| | 20 May/2130 GMT |
| | 21 May/1100 GMT |

Secondly, some releases were either missing altogether (11 occurrences), terminated early, or contained data gaps at various levels because of sonde failure or other difficulties. In addition, although most of the sondes were released within 15 minutes of each other, a few releases were delayed by as much as 30 to 90 minutes. Thus, non–simultaneous releases combined with variations in ascent rates caused the sondes to reach given pressure levels at different times. Fankhauser (1969) has noted that for mesoscale studies, the data must be adjusted so they describe a particular level at the same time.

To deal with these problems, analytical procedures similar to those of Fuelberg and Jedlovec (1982) were utilized. To account for non–simultaneous sonde releases and variable ascent rates, data at each level were adjusted to a common time using a linear interpolation scheme similar to that of Fankhauser (1969). Since the scheduled release times were 55 minutes prior to the standard hour (e.g., 1105 for 1200 GMT), all data were adjusted to the prior hour (e.g., 1100 GMT) and will be denoted as 1100 GMT, 1400 GMT, etc. soundings. To generate values for missing data, linear time interpolation at individual stations was used if two conditions were satisfied. First, interpolation was not employed over a time interval greater than 6 h, and second, extrapolation was avoided by not using the procedure at the first or last times. Approximately 15% of the total soundings used during the 24 h period were created in this way. Table 3 gives a list of avail-

a

Table m   Number of mesonetwork soundings before and after the data generation technique for various pressure levels during AVE-SESAME V. The left value in each column is the number of soundings before generation, whereas the right value is the number after generation.

| Pressure level (mb) | 1100 GMT | 1400 GMT | 1700 GMT | 2000 GMT | 2130 GMT | 2300 GMT | 0200 GMT | 0330 GMT | 0500 GMT | 0700 GMT |
|---|---|---|---|---|---|---|---|---|---|---|
| 150 | 15-15 | 17-18 | 15-15 | 9-13 | 10-11 | 8-5 | 6-8 | 7-8 | 15-15 | 17-17 |
| 200 | 17-17 | 17-18 | 15-15 | 9-1m | 17-11 | 8-1m | 10-12 | 9-13 | 16-17 | 17-17 |
| 300 | 17-17 | 17-18 | 15-15 | 10-14 | 12-13 | 9-10 | 14-10 | 10-14 | 16-17 | 17-17 |
| 500 | 17-17 | 17-18 | 16-16 | 12-16 | 13-16 | 10-16 | 12-17 | 12-17 | 16-17 | 17-17 |
| 700 | 17-17 | 18-18 | 16-16 | 15-16 | 17-16 | 12-17 | 18-18 | 15-18 | 17-18 | 18-18 |
| 850 | 17-17 | 18-18 | 16-16 | 16-16 | 16-17 | 14-18 | 19-19 | 16-18 | 18-18 | 18-18 |

able data before and after the interpolation technique. As a check on the final data set, time series and constant pressure plots were computer generated and hand analyzed. Values that did not appear valid were removed and not used in any further calculations.

After obtaining the time consistent data set, the storm scale values were objectively analyzed onto a 15 x 13 grid using the Barnes (1964) procedure. A grid length of 25 km and a scan radius of 150 km (2 times the average station spacing or 6 grid lengths) were used. Four iterations of the scheme produced the desired resolution. Gridded fields of height, temperature, winds, and dewpoint were obtained at the surface and at 50 mb intervals from 900 to 150 mb. Too much data were missing at 100 mb to permit analysis. Since average sonde drift at 150 mb was approximately 45 km, nearly two grid units, sonde locations at individual levels were determined as part of the analysis procedure and used instead of surface locations, Winds at individual 50 mb levels were averages at that level and 25 mb above and below in order to suppress inherent data errors. A mild filter was applied to all gridded fields (Shuman, 1957) to diminish small waves that could not be adequately resolved.

With an average station spacing of 75 km, unambiguous resolution is restricted to features with wavelengths greater than 150 km (two times the station spacing), Therefore, phenomena with smaller wavelengths should be greatly suppressed. In addition,

since the analysis region is only about 400 km on a side, larger features are only partially resolved by the special network. Figure 2 shows the response curve for the storm scale study. The final grids retain approximately 32% of originally resolved amplitudes at 150 km wavelengths, and 82% at 225 km wavelengths (two and three times the average station spacing, respectively).

The Barnes (1964) analysis technique also was used to prepare gridded fields of the synoptic-scale data. Using a mesh length of 127 km, a scan radius of 371 km, and four iterations, the values were objectively analyzed onto a 15 x 13 grid. Procedures were similar to those described previously for the special network. The resolution profile for the synoptic-scale data also is shown in Fig. 2.

d. Computational procedures

Since details of the procedures used here are given by Fuelberg and Jedlovec (1982), they will only be summarized in this report. The kinematic method was used to determine vertical motion ($\omega$). The lower boundary condition, normally assumed zero on the synoptic scale, was computed as the sum of three processes: local change of surface pressure, cross-isobaric flow, and terrain-induced vertical motion. A limitation of the kinematic method is that inaccuracies in the winds accumulate during the integration of divergence so that unrealistic magnitudes of $\omega$
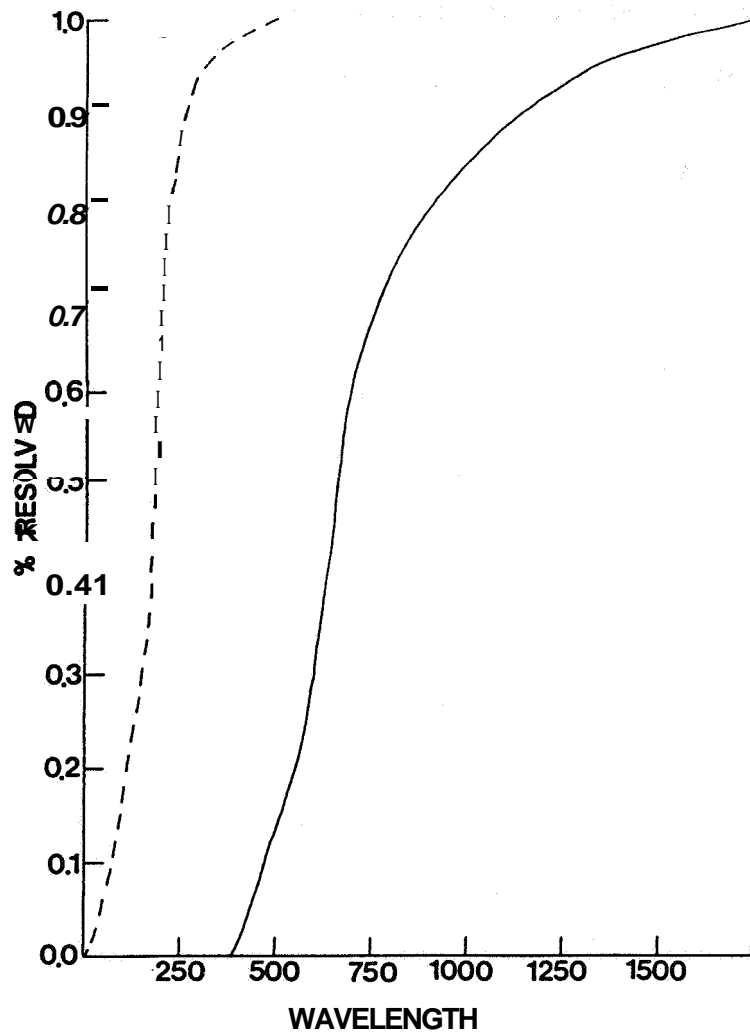
19

Fig. 2.  Response curves for the meso β-scale (dashed) and
         synoptic-scale (solid) gridded fields.  Wavelengths
         are in km.

occur near 150 mb. To circumvent this problem, values of both $\omega$ and horizontal divergence were modified using O'Brien's (1970) adjustment scheme. This procedure forces the vertical motion to a predetermined value at 150 mb. Then, values of divergence are altered by amounts that would produce the modified $\omega$ profiles. Our original goal was to set kinematic motions at 150 mb equal to values obtained from the adiabatic method. Adiabatic motions can be obtained independently of the kinematic results and were hypothesized to be more realistic than an assumption of zero which is normally used. Unfortunately however, trial adjustments to adiabatic values did not produce reasonable results, apparently because the intense convection produced significant latent heat release that greatly violated the adiabatic assumption. Therefore, vertical motions were adjusted to zero at 150 mb in the usual manner.

Terms of the kinetic energy budget equation were computed using horizontal and vertical centered finite differences at the 17 levels. These values then were integrated over 50 mb layers by means of the trapezoidal rule. Dissipation was calculated as a residual from the other terms in (1). The use of non-centered time differences for calculating, $\partial K / \partial t$ was investigated. However, this method is somewhat unsatisfactory since a complete energy budget is not produced at every observation time. Results showed that values of both $\partial K / \partial t$ and dissipation generally were not affected greatly by the type of time differencing employed.

Therefore, centered finite differences were used. The only exceptions were at the first and last times and when the 2130 GMT observation required an uncentered procedure.

e. **Error** analysis

Uncertainties in rawinsonde data are mainly due to random error. systematic error, and aliasing. The data handling and computational schemes described earlier should greatly reduce the effects of these errors on the energy budget calculations; however. they will not be completely suppressed. Therefore, it is imperative to determine quantitative confidence limits for the derived parameters. Unfortunately, there is no effective procedure to test for systematic errors; therefore, this type of uncertainty was not considered. In addition, data limitations and computational inadequacies such as truncation error were not evaluated. On the other hand, the effects of random errors on the energy analyses were documented using randomly perturbed data. The procedures utilized in this analysis, as well as detailed results, are presented in the Appendix. Briefly stated, however, the findings indicate that errors in rawinsonde data should not significantly affect the interpretations of results that follow.

## 3. WEATHER CONDITIONS

Although the AVE-SESAME I period has been the subject of many studies because it coincided with the Red River Valley tornado outbreak, the fifth SESAME case (20-21 May 1979) also was a period of significant convective activity. During the 24 h period beginning at 1200 GMT 20 May, a total of seven tornadoes, one funnel cloud, and several hook echoes were documented within the overall synoptic-scale network (July and Turner, 1981). In addition, there were numerous occurrences of hail. Although no tornadoes were reported within the meso β-scale storm network, thunderstorm activity was intense, and rainfall amounts exceeded 3 in. at several sites. This section highlights weather conditions of the storm scale network during AVE–SESAME V; however, a more detailed account is given by Fuelberg and Printy (1983).

Synoptic conditions at the beginning of the experiment (1200 GMT 20 May) are shown in Fig. 3. At the surface, a relatively strong cold front extended from the Great Lakes into the Ohio Valley. From there it became stationary, winding through central Oklahoma and into New Mexico. Conditions in the upper troposphere were dominated by a cut-off low centered just south of Arizona and its major trough extending northeastward. A short wave trough was situated in the upper Midwest. Jet maxima were located over the Iowa–Minnesota border and south of the cut-off low over northern Mexico. Winds were generally light over Oklahoma and northern
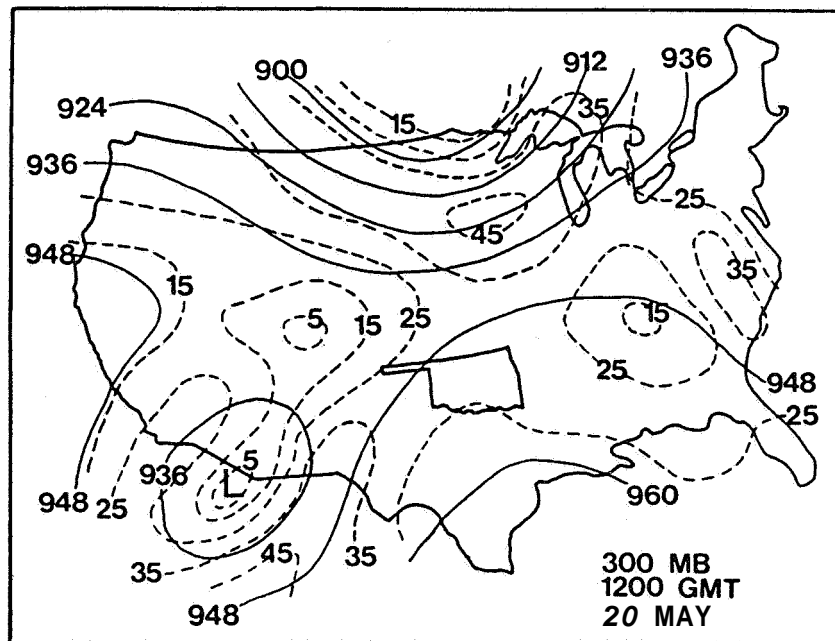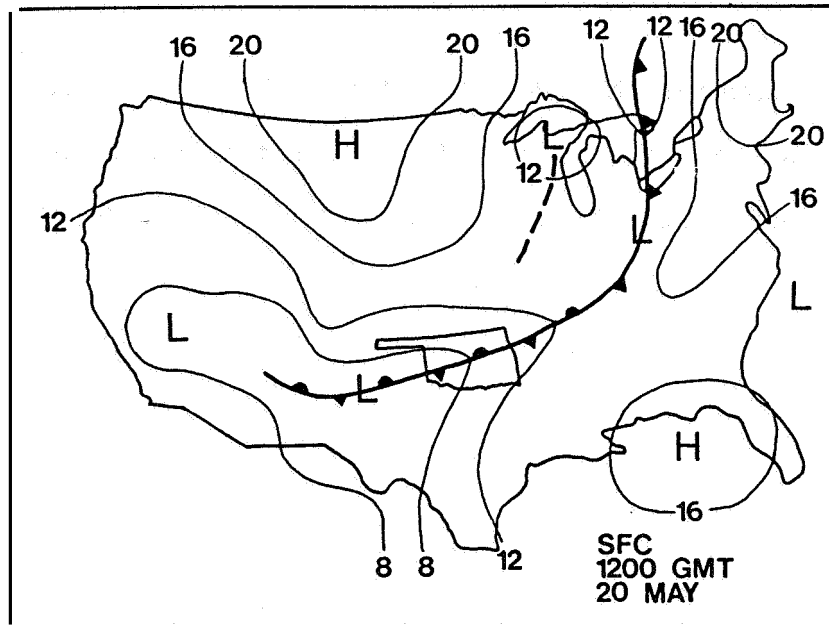
Fig. 3. Surface and 300 mb National Meteorological Center (NMC)
analyses for 1200 GMT 20 May 1979. Isotachs (dashed)
are in m s$^{-1}$.

Texas. Precipitation was occurring north of the front, covering a broad area of Missouri, northern Arkansas, and eastern sections of Kansas and Oklahoma. Echo tops of thunderstorms reached 17.1 km (56,000 ft), and rainfall totals of 1-2 in. occurred in these areas during the early morning hours. The storms had moved eastward, out of Oklahoma by 1500 GMT when they were situated over Arkansas and southern Missouri.

The front gradually moved southeastward during the day, and by 1700 GMT, it extended from near Stroud (SUD) in northeastern Oklahoma to near Shamrock (SHM) in the Texas panhandle. The atmosphere south of the front was quite unstable by midday. At 1700 GMT, values of the Total Totals and K indices were generally in the lower 60's and upper 30's, respectively, while Lifted Indices were near -6. This instability coupled with afternoon heating and frontal lifting provided the necessary conditions for intense convective activity.

Radar summaries for the peak storm period are given in Fig. 4. In addition, constant pressure maps for the meso β-scale region are presented in Figs. 5-6 for 850 and 200 mb, respectively. Just prior to convective development (1700 GMT), the 850 mb chart depicts a low over the Texas panhandle and a slight ridge over central Oklahoma. Winds were weak but exhibited considerable cyclonic turning. The 200 mb height contours were generally smooth, showing no major perturbations. Southwesterly winds contained very little diffluence.
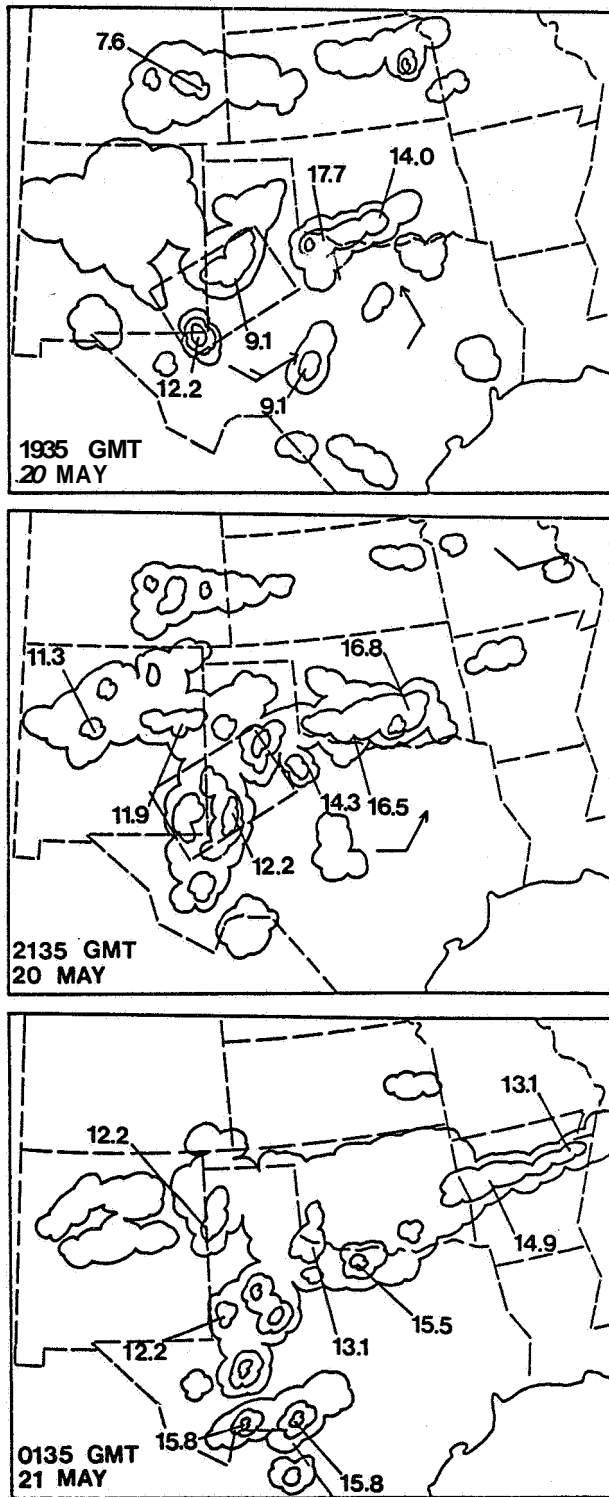
Fig. *4* NMC radar summaries with echo tops in km and speeds in m s$^{-1}$.
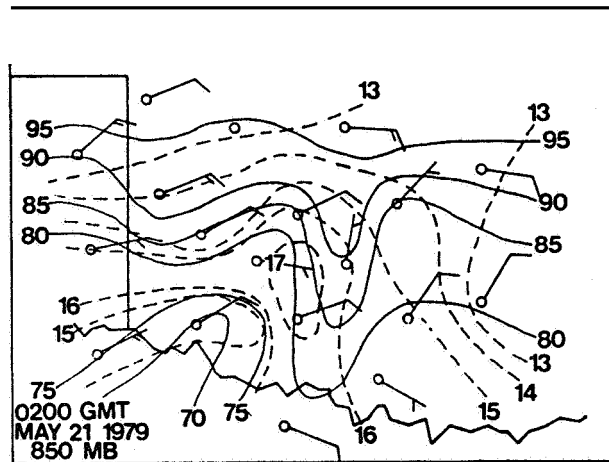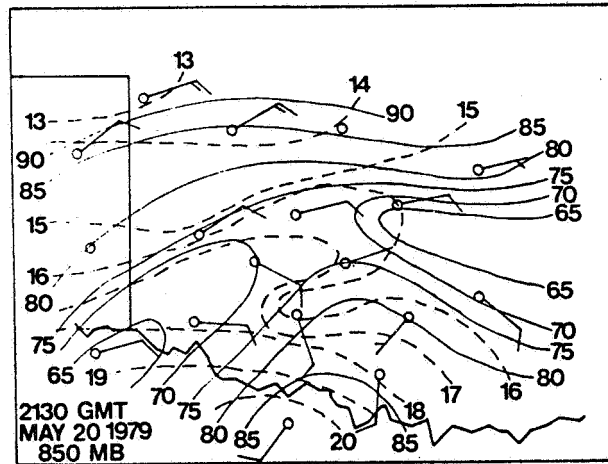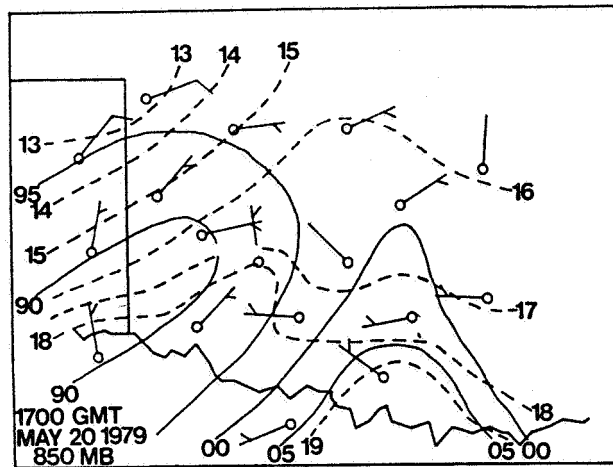
Fig. 5.  850 mb height analyses in 5 m intervals (solid); 00
means 1500 m.  Winds are in m s$^{-1}$ with short barbs
denoting 5 m s$^{-1}$.  Isotherms (dashed) are in °C.

27
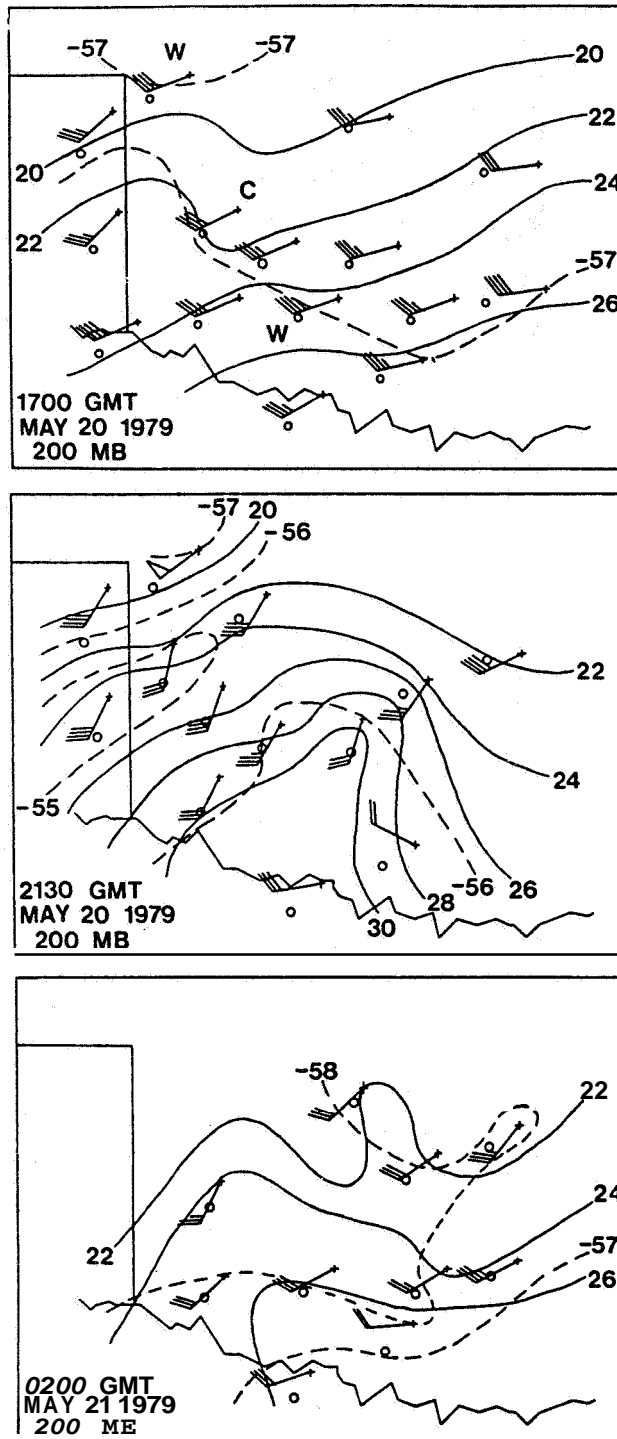
Fig. 6. *200* mb height analyses in 20 m intervals (solid); *24* means *12,240* m. Winds are in m s$^{-1}$ with short barbs denoting 5 m s$^{-1}$. Isotherms (dashed) are in °C. Surface station locations are given by circles although data are plotted at the *200* mb sonde locations that are indicated by crosses.

Convection **first** formed along the front near **1700** GMT, and by 1935 GMT, a well defined area of storms extended from near Childress, TX (**CDS**) to Ada, OK (**ADA**) (Fig, 4). The strongest cells were located between Childress and Wichita Falls, TX (**SPS**). **Maximum** echo tops in this region reached 17.7 km (58,000 ft), and hail was reported near Ada. Figure 7 shows the extent of cloud cover over the mesonetwork at 2026 GMT, The intense convection appeared to be most widespread near 2135 GMT (Fig. **4)**. Radar reports from Oklahoma City (**OKC**) at 2330 GMT indicated that level 4 thunderstorms (**TRW++**) **still** covered most of Oklahoma and **north-** **central** Texas. By **0135 GMT,** light rain persisted over Oklahoma as the heavy storm cells moved eastward into Arkansas. However, other strong storms were nearby, situated just south of the special network along the Red River Valley.

Significant changes in the atmosphere occurred during peak storm activity, and these are clearly seen on the constant pressure maps (Figs. **5-6**). Surface pressures (not shown) fell over most of the network between 1700–2130 GMT. Greatest decreases of 3–5 **mb** were located in the southeastern half of the data region. Consequently, height falls **of** 20–40 m at **850** mb (Fig. 5) are common over southeastern Oklahoma during the 4.5 h period. This results in a pronounced trough from near KTVY (TVY) to near **Chil-** dress (CDS). Winds at several stations in the southeastern part of the network have shifted to a more southerly direction, thereby supplying warm, moist air into the convective area. At 200 **mb**
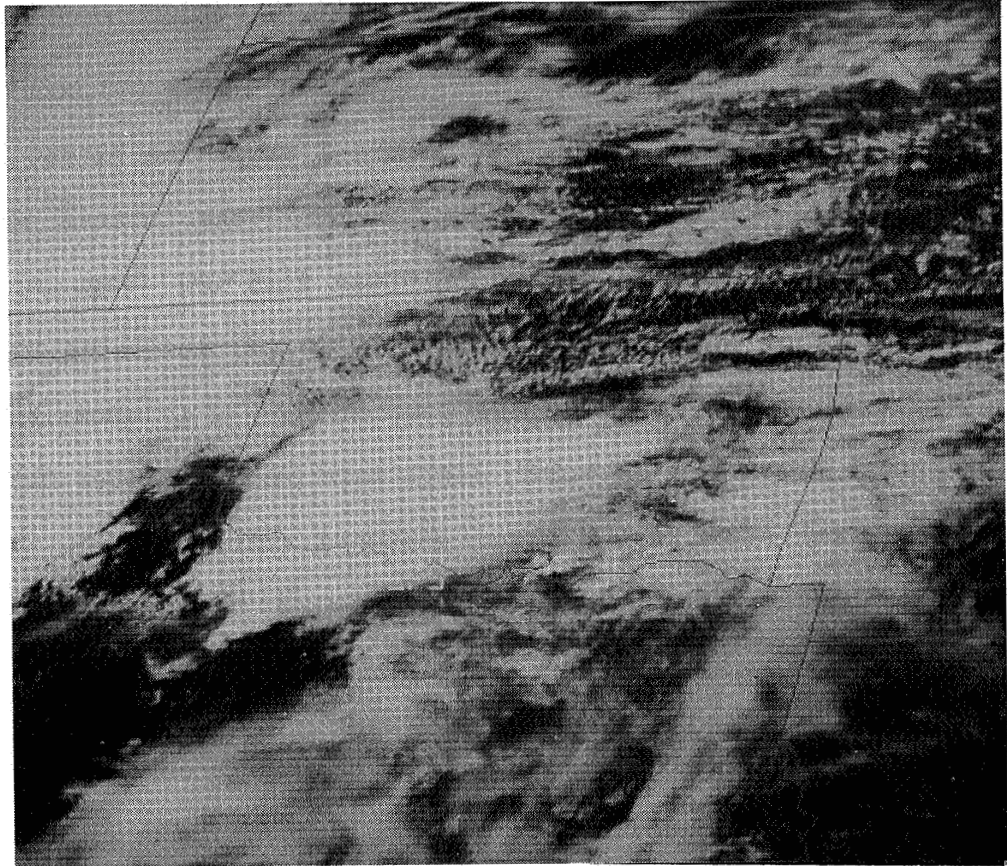
Fig. 7. Goes visible image at 2026 GMT 20 May.

(Fig, 6), significant warming and ridging has occurred in close proximity to the storm area. Winds now show pronounced diffluence and strongly ageostrophic flow. Maps at 0200 GMT suggest that the region was returning to pre-storm conditions. Temperature and height patterns at 850 mb still are rather disturbed; however, at 200 mb, the ridging has greatly diminished, and diffluence is much less pronounced.

Strong variability within the meso B-scale storm environment can be seen in pressure-time cross sections of horizontal divergence and vertical motion (Figs. 8 and 9, respectively). These diagrams represent area-averaged values for the innermost 13 x 11 grid points of the total analysis region. The time series for horizontal divergence depicts the rapid development of pronounced low level convergence and upper level divergence after the convection began shortly after 1700 GMT. Greatest values coincide with the times of peak storm activity. These findings are consistent with those observed on the constant pressure maps, i.e., strong inflow at 850 mb and diffluence at 200 mb. Values decreased after 0200 GMT as the intense storms were replaced by rainshowers. Strong mesoscale ascent developed in response to the wind flow (Fig. 9). Although maximum area-averaged vertical motion was $-22$ $\mu b\ s^{-1}$ near 400 mb at 2130 GMT, horizontal cross sections for that time (not shown) indicate that values at individual grid points exceeded $-60\ \mu b\ s^{-1}$.

During the last half of the experiment period, the cut-off

31
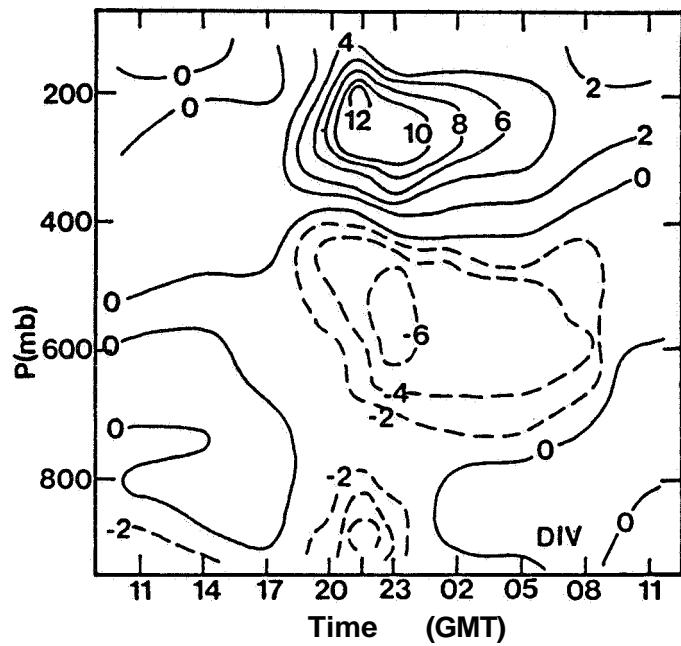
Fig. 8. Pressure-time cross section of horizontal
divergence ($10^{-5}$ $s^{-1}$) for the inner 13 x 11
grid area of the total analysis region.
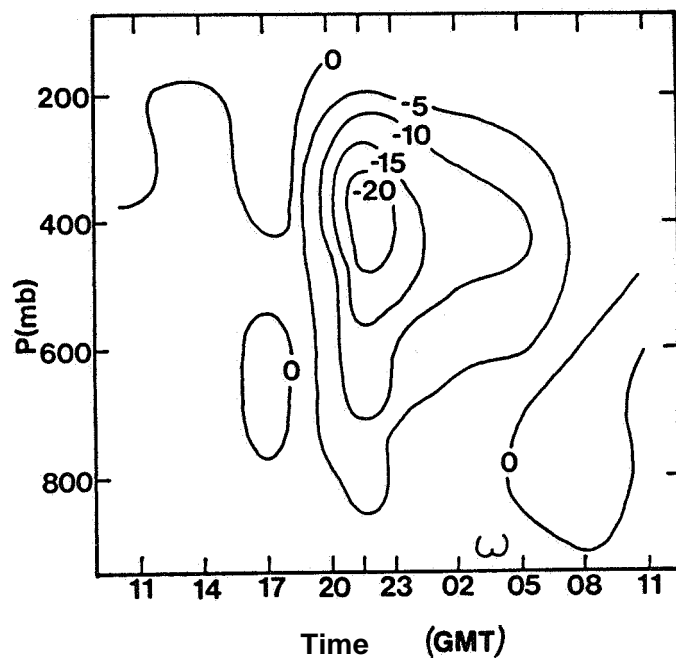
Fig. 9. Pressure-time cross section of vertical motion
($\mu$b s$^{-1}$) for the inner 13 x 11 grid area of the
total analysis region.

low in the upper levels moved slightly northeastward toward the Arizona–New Mexico border. The front advanced southeastward with continuing isolated severe convective activity nearby. By 1200 GMT 21 May, the end of the period, the cold front had become stationary over central Texas. Although storm intensities had decreased, convective activity continued over Texas, Oklahoma, Arkansas., and southern Kansas.

# 4. RESULTS

This section will describe the kinetic energy balance of the meso β-scale' network. Area-averaged energetics will be discussed first, followed by a description of its time variability. Next, horizontal maps of kinetic energy budget terms will be presented to explain flow patterns within the storm scale environment, Finally, the energetics of a subregion over the southeastern portion of the network will be isolated to diagnose possible causes of upper level wind variations that are observed during the times of intense storm activity.

a. &ea-time averaged enernetics

Terms of the kinetic energy budget equation were evaluated for each observation time at individual grid points. Integrated grid point values were averaged over the energy analysis region in Fig, **1.** Area-averaged results for the ten times then were combined to produce the composite area-time averaged energy budget which is given in Table 4.

Kinetic energy content for the surface to 150 mb column is 11.99 x $10^5$ J $m^{-2}$, with the major contribution coming from near jet stream level. All levels experience a net decrease of kinetic energy during the 24 h period, with the vertical total being -5.41 W $m^{-2}$. This local change is due to various sources, sinks, and

Table 4. Area-time averaged meso β-scale kinetic energy budget for the AVE-SESAME 3 period. Values of K are $10^5$ J m$^{-2}$ while others are W m$^{-2}$.

| Pressure Layer (mb) | K | $\partial K/\partial t$ | $-\vec{V}\cdot\vec{\nabla}\phi$ | $-\vec{V}\cdot k\vec{V}$ | $-\partial\omega k/\partial p$ | D | $-\vec{V}\cdot\vec{\nabla}k$ | $-k(\vec{\nabla}\cdot\vec{V})$ |
|---|---|---|---|---|---|---|---|---|
| 200–150 | 2 35 | -0 06 | 18 99 | -11 26 | 5 96 | -14 15 | -1 84 | -9 02 |
| 300–200 | 4 40 | -1 56 | 33 20 | -28 02 | 8 52 | -15 26 | -8 17 | -19 85 |
| 400–300 | 2 29 | -0 50 | 18 52 | -10 57 | -2 74 | -5 71 | -3 42 | -7 15 |
| 500–400 | 1 02 | -0 31 | 6 82 | 0 52 | -6 02 | -1 63 | -0 25 | 0 77 |
| 600–500 | 0 74 | -0 54 | 2 20 | 1 67 | -3 11 | -1 30 | 0 19 | 1 48 |
| 700–600 | 0 38 | -0 40 | 1 25 | 0 57 | -1 79 | -0 43 | -0 04 | 0 61 |
| 800–700 | 0 25 | -0 82 | -0 18 | -0 32 | -0 18 | -0 14 | -0 32 | 0 00 |
| 900–800 | 0 36 | -0 79 | 0 97 | -0 3a | -0 02 | -1 38 | -0 40 | 0 08 |
| SFC–900 | 0 20 | -0 03 | 1 80 | 0 38 | -0 59 | -1 62 | 0 10 | 0 28 |
| Vertical Total | 11 99 | -5 41 | 83 57 | -47 39 | 0 03 | -41 62 | -10 19 | -33 20 |

transports. Generation of kinetic energy by cross−contour flow, which produces a vertical total of 83.57 W $m^{-2}$, is the dominant source to the region. Energy generation occurs within most layers but is greatest above 400 mb. A secondary maximum exists I.. the planetary boundary layer.

Horizontal flux divergence and dissipation are major sinks of kinetic energy. Vertical totals for these terms are −47.39 W $m^{-2}$ and −41.62 W $m^{-2}$, respectively. Again, the processes are largest in the upper levels of the atmosphere. The vertical profile of dissipation is similar to that of generation, i.e., a maximum near jet stream level, weak dissipation in the mid−troposphere, and another maximum near the surface. Significant horizontal outflow exists in the upper troposphere (negative values), while weaker horizontal inflow occurs in the middle layers.

To further investigate the physical mechanisms creating horizontal flux divergence, the term was separated into two components

$$-\vec{\nabla} \cdot k\vec{V} = -\vec{V} \cdot \vec{\nabla}k - k(\vec{\nabla} \cdot \vec{V}).$$ (2)

The first term on the right represents horizontal advection of kinetic energy, while the second signifies flux due to horizontal divergence. Table 4 shows that both components produce an energy sink above 400 mb; however, outflow due to velocity divergence is the dominant process.

Values of vertical flux divergence (Table 4) indicate an

37

export of energy in the lower and middle layers with significant import above 300 mb. This is consistent with the widespread ascending motion that characterizes much of the fifth SESAME period. The small total exists because vertical motions at 150 mb were adjusted to zero, whereas surface values were not.

Current results now will be compared with those of Tsui and Kung (1977), hereafter denoted as T & K. Direct comparison with their study is possible since the resolution of their NSSL input data is very similar to that of the present investigation (meso β–scale). To the authors' knowledge, the energetics of no other periods have been investigated at such a fine resolution. (McInnis and Kung (1972) and Kung and Tsui (1975) considered the same days as T & K.) T & K computed energy budgets on nine days. These were categorized according to the particular type of storm conditions that occurred, i.e., convective, non–convective, or frontal. Four days were labeled as convective because active storms were identified in the network along with strong, upward vertical motions. Three days were classified as non–convective since storms were either weak or failed to develop within the network area. Finally, two days were characterized by their association with cold fronts, either by the presence of a prefrontal squall line or by frontal passage through the analysis region. The development of convective activity in both cases, however, was limited. Table 5 presents composite kinetic energy budgets for T & K's categories along with current results.

Table 5. Mean kinetic energy budget in various types of storm situations (Tsui and Kung, 1977). Current results also are given. Values of K are $10^5$ J m$^{-2}$ while others are W m$^{-2}$.

| Type | Pressure Layer (mb) | K | $\partial K/\partial t$ | $-\vec{\nabla}\cdot k\vec{V}$ | $-\partial\omega k/\partial p$ | $-\vec{V}\cdot\vec{\nabla}\phi$ | D |
|---|---|---|---|---|---|---|---|
| Convective | 400-100 | 12.54 | 0.68 | -6.03 | 14.70 | 61.88 | -69.88 |
| | 700-400 | 6.04 | 1.58 | 11.84 | -11.63 | 13.03 | -11.67 |
| | 1000-700 | 2.44 | 2.36 | 5.14 | -2.87 | 14.54 | -14.45 |
| | Total | 21.02 | 4.62 | 10.96 | 0.20 | 89.45 | -95.99 |
| Non-convective | 400-100 | 6.54 | -0.59 | -2.88 | -0.76 | -31.61 | 34.66 |
| | 700-400 | 1.38 | -1.12 | -0.46 | 0.59 | -13.26 | 12.01 |
| | 1000-700 | 1.59 | 1.93 | -1.28 | 0.19 | 9.97 | -6.95 |
| | Total | 9.50 | 0.21 | -4.63 | 0.01 | -34.89 | 39.72 |
| Frontal | 400-100 | 3.29 | -0.13 | -2.59 | 3.12 | 0.50 | -1.15 |
| | 700-400 | 2.56 | -2.95 | 0.85 | -2.04 | 1.50 | -3.26 |
| | 1000-700 | 1.20 | -1.82 | 0.16 | -1.00 | 13.04 | -14.03 |
| | Total | 7.05 | -4.90 | -1.58 | 0.08 | 15.04 | -18.44 |
| AVE-SESAME 3 | 400-150 | 9.04 | -2.52 | -49.85 | 11.74 | 70.71 | -35.12 |
| | 700-400 | 2.14 | -1.25 | 2.76 | -10.92 | 10.27 | -3.36 |
| | Sfc-700 | 0.81 | -1.64 | -0.30 | -0.79 | 2.59 | -3.14 |
| | Total | 11.99 | -5.41 | -47.39 | 0.03 | 83.57 | -41.62 |

T & K's convective category was the most energetically active. Vertical totals of generation on individual days ranged from 73.00 to 110.14 W m$^{-2}$. The four day average was 89.45 W m$^{-2}$ (Table 5). Dissipative losses tended to balance generation; vertical totals ranged from -14.08 to -200.44 W m$^{-2}$, for a mean value of -95.99 W m$^{-2}$. A significant amount of kinetic energy was transported into the upper troposphere. Horizontal inflow existed in the middle and lower layers, whereas weaker values of flux divergence occurred in the 400-100 mb layer.

Although a cold front was located in the mesonetwork during most of the AVE-SESAME V period, current energy results are very similar to those of T & K's convective category (Table 5). The current vertical total for generation (83.57 W m$^{-2}$) agrees closely with their average value (89.45 W m$^{-2}$). On the other hand, energy dissipation during AVE-SESAME V (-41.62 W m$^{-2}$) is approximately half that obtained by T & K (-95.99 W m$^{-2}$), but both represent significant losses either by traditional frictional processes or by transfers of energy to unresolvable scales of motion. Vertical profiles of these terms are similar for both studies, i.e., large values near jet stream level, smaller values in the midtroposphere, and secondary maxima near the surface. The current level of kinetic energy content (11.99 x 10$^5$ J m$^{-2}$) is approximately half that of T & K (21.02 x 10$^5$ J m$^{-2}$). Although magnitudes of local change are comparable, the AVESESAME V region experiences decreasing energy content, opposite that of T & K.

Finally, horizontal flux is a major sink for the current study, whereas it provides an important source for T & K. These contrasts are probably attributable to differing locations of' wind maxima between the two studies.

Composite energetics of T & K's non-convective category differs significantly from that of the convective periods and the current investigation (Table 5). The greatest contrasts are in the non-convective processes of cross-contour destruction and positive dissipation (energy supply from unresolvable scales of motion). Although energy processes for the frontal category agree in sign with those of the present study, frontal magnitudes are much weaker. This probably occurs because the convection during AVE–SESAME V was more intense than that during T & K's frontal days.

Since data were simultaneously collected at both the synoptic and meso β-scales during AVE–SESAME V, we have a unique opportunity to compare the energetics of the same analysis region derived from different scales of input. Previous mesoscale energy investigations (McInnis and Kung, 1972; Kung and Tsui, 1975; Tsui and Kung, 1977) did not have the corresponding 3 h synoptic–scale data; therefore, to the authors' knowledge, this type of comparison has never been previously reported in the literature. Using methods similar to those of Fuelberg and Jedlovec (1982), the synoptic–scale energy budget was evaluated at individual grid points for each observation time. Next, grid point values were

averaged within a $6.4 \times 10^4$ km$^2$ area over Oklahoma which agrees closely in both size and location with the meso β-scale region in Fig, 1. The resulting composite area–time averaged budget is given in Table 6.

There are many similarities between results from the two resolutions. Although energy processes dominating the meso β-scale storm environment usually characterize the larger scale flow, magnitudes at the finer resolution often are considerably greater, Closest agreements are found in energy content and its local derivative. The total for synoptic–scale kinetic energy content $(13.20 \times 10^5$ J m$^{-2})$ compares favorably with the meso B-scale value $(11.99 \times 10^5$ J m$^{-2})$, and vertical distributions show corresponding similarities. In addition, each area experiences a local decrease in energy during the 24 h period.

Cross–contour generation (Table 6) is much larger at the meso β-scale (83.57 W m$^{-2}$ versus 30.62 W m$^{-2}$), probably due to the enhanced ability of the denser network to detect the strongly ageostrophic flow of the storm environment. Magnitudes of synoptic–scale dissipation are more comparable to those from the special sites. Horizontal transport at the synoptic scale is near zero. As a result, most of the energy generated within the region is transferred to unresolvable scales of motion. On the other hand, strong horizontal outflow is detected at the meso β-scale, particularly in the 400–150 mb layer. Upward transport also is considerably stronger at the meso (3-scale. The greater magnitudes

42

Table 6. Area-time averaged kinetic energy budgets for the synoptic- and meso β-scales. Values of K are $10^5$ J m$^{-2}$ while others are W m$^{-2}$.

| Type | Pressure Layer (mb) | K | $\partial K/\partial t$ | $-\vec{\nabla}\cdot k\vec{V}$ | $-\partial\omega k/\partial p$ | $-\vec{V}\cdot\vec{\nabla}\phi$ | D |
|---|---|---|---|---|---|---|---|
| Synoptic-scale[a] | 400-150 | 10 32 | 0 95 | -1 68 | 6 78 | 25 61 | -29 76 |
| | 700-400 | 2 16 | -2 57 | 0 92 | -5 91 | 3 13 | -0 71 |
| | Sfc-700 | 0 72 | -2 17 | 0 95 | -0 85 | 1 88 | -5 18 |
| | Total | 13 20 | -3 79 | 0 19 | 0 02 | 30 62 | -34 62 |
| Meso β-scale[a] | 400-150 | 9 06 | -2 52 | -49 85 | 11 74 | 70 71 | -35 12 |
| | 700-400 | 2 05 | -1 25 | 2 76 | -10 92 | 10 27 | -3 36 |
| | Sfc-700 | 0 81 | -1 64 | -0 30 | -0 79 | 2 59 | -3 14 |
| | Total | 11 99 | -5 41 | -47 39 | 0 03 | 83 57 | -51 62 |

43

of both flux terms at the smaller scale are due to at least three factors, First, since velocity divergence is highly scale dependent, horizontal transports at the finer resolution will be enhanced. This factor also produces greater vertical motions at the storm scale. Second, the special network better resolves small scale wind phenomena which are accompanied by strong horizontal gradients of kinetic energy, Finally, area-averaged energy content is greater at the meso $\beta$-scale. Thus, it appears that contrasts in results are mainly attributable to differences in resolution between the two data networks.

Table 7 presents results from several previous studies of convective environments derived from synoptic-scale input data, Values from T & K's convective category and the current investigation are included for easy reference. The energetics in the vicinities of two squall lines (areas approximately $11 \times 10^5$ km$^2$) (Fuelberg and Scoggins, 1978) are most similar to current values, Generation by cross-contour flow is the greatest source in both studies while horizontal outflow and dissipation are major sinks. Investigations by Robertson and Smith (1980) and Fuelberg and Jedlovec (1982) considered much larger regions of the nation, and their results differ considerably from those of AVE-SESAME V, Judging from the wide variation in values from the larger areas, it appears that severe storm outbreaks can occur among many different types of energy balances. This is attributable to the varying types of flow patterns associated with intense convection.

Table 7. Vertically integrated area-averaged kinetic energy budgets for various case studies. Values of K are $10^5$ J m$^{-2}$ while others are W m$^{-2}$.

| Study | Scale | K | $\partial K/\partial t$ | $-\vec{V}\cdot\nabla\phi$ | $-\vec{V}\cdot k\nabla$ | $-\partial\omega k/\partial p$ | D |
|---|---|---|---|---|---|---|---|
| Fuelberg and Scoggins (1978) 2 Squall-line Vicinities | synoptic 3 and 6 h | zU T | -7 7 | 23 4 | -15 z | 0 2 | -16 1 |
| Fuelberg and Jedlovec (1982) AVE-SESAME I | meso α 3 h | 35 U | 16 6 | -5 8 | 21 3 | 0 1 | 1 0 |
| Robertson and Smith (1980) Palm Sunday 1965 Outbreak | synoptic 12 h | z8 T | 6 7 | -z7 6 | 25 6 | 0 0 | 8 T |
| Robertson and Smith (1980) Jumbo 1974 Outbreak | synoptic 12 h | 3U 7 | U 5 | 4 T | 21 2 | 0 0 | -z1 U |
| Tsui and Kung (1977) Convective cases | meso β 1.5 h | 21 0 | U 6 | 89 U | 11 0 | 0 2 | -96 0 |
| Current study | meso β 1.5 and 3 h | 12 0 | -5 U | 83 6 | -UT U | 0 0 | -U1 6 |
| Current study Synoptic subregion | synoptic 3 h | 13 Z | -3 8 | 30 6 | 0 2 | 0 0 | -3U.6 |

On the other hand, results from AVE–SESAME V, T & K, and Fuelberg and Scoggins (1978) imply that the near storm environment may often be characterized by strong generation and negative dissipation, regardless of whether synoptic or mesoscale data are employed.

Previous studies have suggested that values of energy budget terms undergo major time variations that are related to the presence and strength of nearby storms (McInnis and Kung, 1972; Kung and Tsui, 1975; Tsui and Kung, 1977; Fuelberg and Scoggins, 1978). Since intense convection occurred within the AVE–SESAME V network between 2000–0200 GMT, it is informative to examine current energy variability. Time series of surface–150 mb totals and pressure-time cross sections are presented for this purpose.

The time series (Fig. 10) shows that the meso $\beta$-scale region (Fig. 1) experiences a decrease of kinetic energy content through most of the 24 h period. The greatest drop occurs during the times of strongest convective activity (2000–0200 GMT) when values decrease 4.43 $\times$ $10^5$ J $m^{-2}$. The pressure-time cross section of the local change term (Fig. 11) indicates that most of this decrease occurs above 300 mb. Interestingly, however, a center of increases is located near 400 mb. This vertical variation will be discussed in greater detail in Section 4c. It agrees with findings of Vincent and Carney (1982) who observed decreases in jet level winds accompanied by the formation of a mid–level wind maximum during the Red River Valley tornado outbreak. T & K also observed a
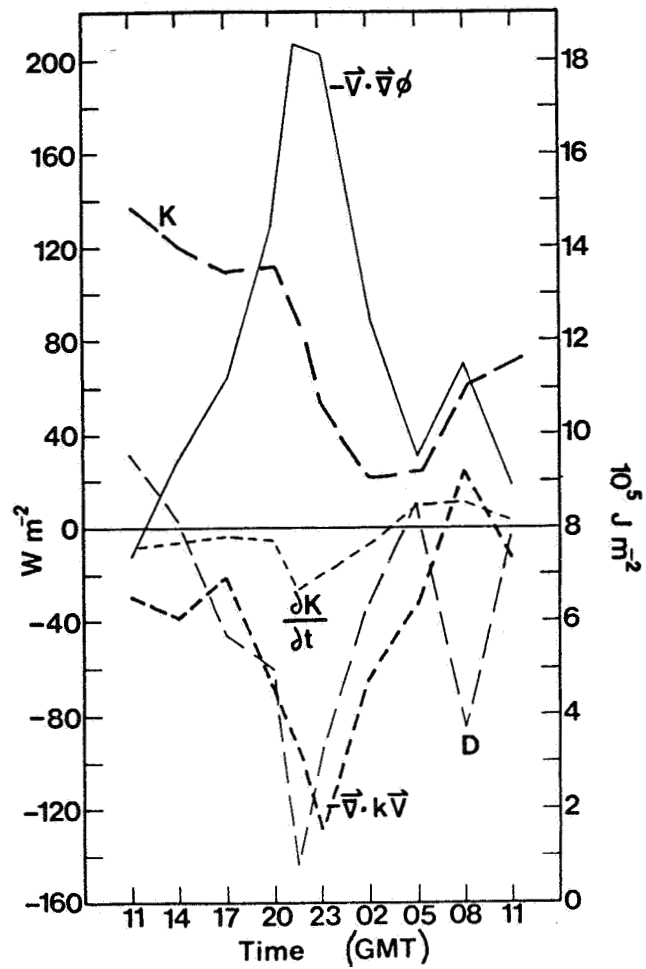
46

Fig. 10. Time series of meso 8-scale energy budget terms integrated between the surface and 150 mb. Three hour time intervals are indicated on the horizontal axis.
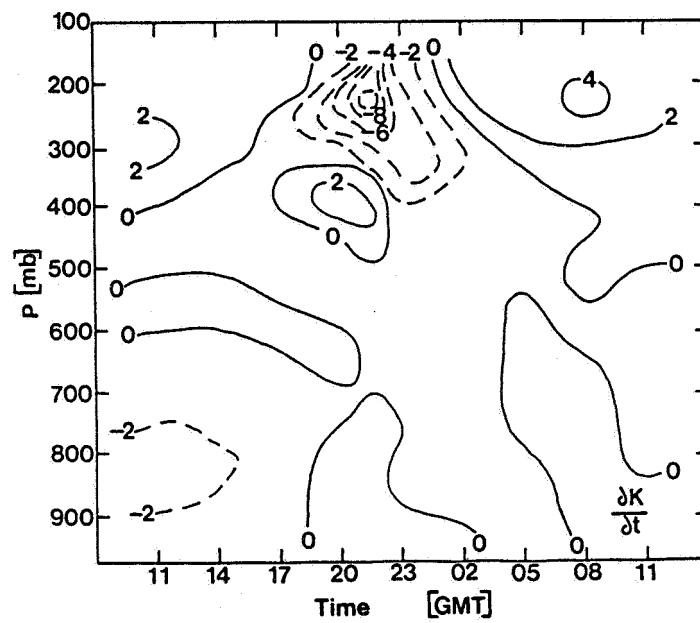
47

a

Fig. 11. Pressure-time cross section of area-averaged local change of kinetic energy. Units are $W\ m^{-2}/50\ mb$.

buildup of mid-level energy prior to peak storm activity, but contrary to current results, energy increases also were observed above 400 mb. The increases near 0800 GMT (Figs. 10-11) are due to jet intrusion into the network from the south. This feature will be described further in Section 4b.

Vertical totals of cross-contour generation (Fig. 10) show major variations during the 24 h period. Values range from -11.6 W m$^{-2}$ at the initial observation time to a maximum of 208.98 W m$^{-2}$ at 2130 GMT. By **0500** GMT magnitudes drop to near pre-storm conditions. The pressure-time cross section (Fig. 12) shows that largest variability occurs above 400 mb and **is** centered about the time of greatest storm activity (2130 GMT). This extreme amount of upper level generation **is** attributable to strongly divergent flow being superimposed on a mesoridge (Fig. 6). Another interesting feature **is** the area of weak destruction that exists in the middle troposphere near 2130 GMT. T & K found significant energy generation prior to and after thunderstorm passages, whereas cross-contour destruction existed within virtually the entire column at peak intensity. They suggested that generation surrounded the intense storm area while destruction occurred within the area. For the present **SESAME** case, however, destruction **is** limited to the middle layers only and **is** much weaker. Thus, the findings of T & K do not appear to represent all meso β-scale storm environments.

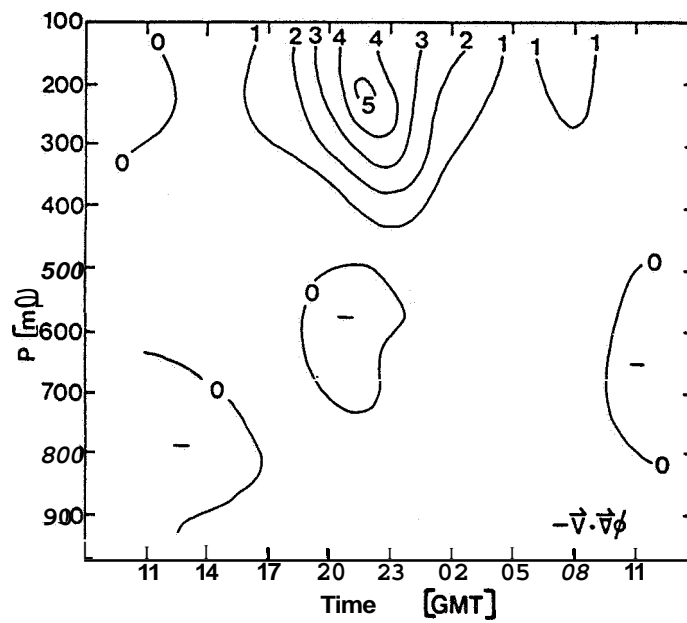Figures 10 and **13** show that dissipation also undergoes major

49

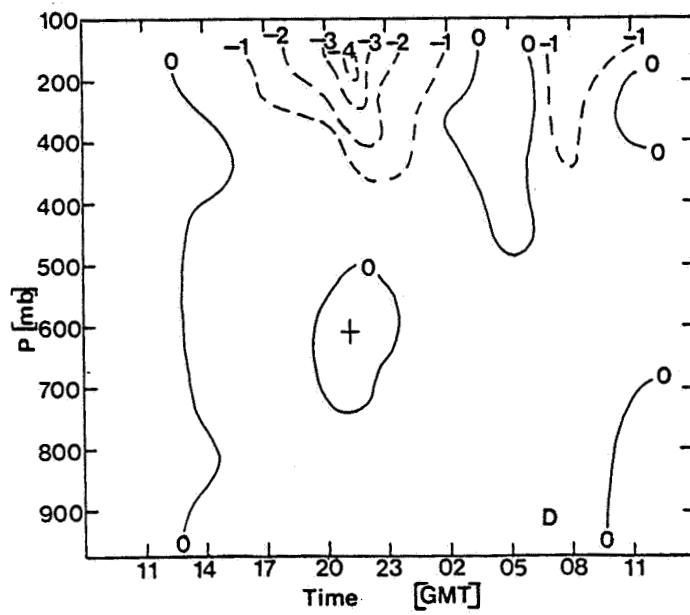Fig. 12. Pressure-time cross section of area-averaged generation of kinetic energy. Units are $10^1$ W m$^{-2}$/50 mb.

50

Fig. 13.  Pressure-time cross section of area-averaged
dissipation of kinetic energy.  Units are 10
W m$^{-2}$/50 mb.

fluctuations during the 24 h period. Greatest negative values occur in the upper troposphere centered about 2130 GMT. The secondary maximum at 0800 GMT is associated with the jet intrusion. Patterns and magnitudes are quite similar to those of generation (Fig. 12), i.e., transfers to unresolvable scales (negative dissipation) correspond with cross-contour generation and vice versa. A similar agreement was observed by T & K. Large negative dissipation suggests that much of the kinetic energy generated at the meso β-scale by thunderstorm-induced environmental modification is transferred to scales of motion that are not adequately resolved by the special network. This transfer can either be to subgrid scales or to larger features which are poorly depicted by so small a data area. Finally, one should note the area of weak positive values in the middle troposphere near 2130 GMT. T & K observed a similar, although deeper and more intense, feature during their convective cases, and it has been described during synoptic-scale studies of convective environments as well (Vincent and Schlatter, 1979).

Horizontal flux divergence provides a major energy sink (Fig. 10) during the times of intense convection. The pressur— time cross section (Fig. 14) indicates that this process is greatest in the upper troposphere where values exceed $-40$ W $m^{-2}/50$ mb. Consistent with the intense upward motion between 2000–2300 GMT, the cross section of vertical flux (Fig. 15) shows large upward transport of energy.

a

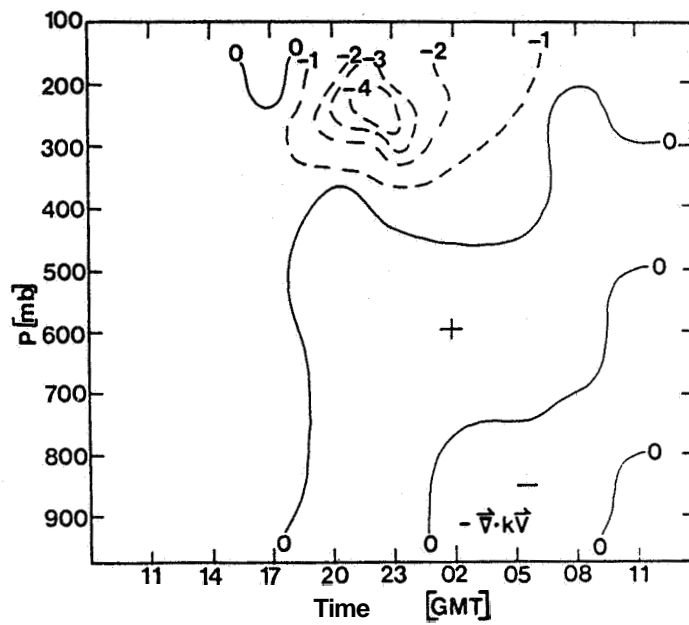Fig. *14.* Pressure-time cross section of area-averaged horizontal flux divergence of kinetic energy. Units are $10^1$ W m$^{-2}$/50 mb.
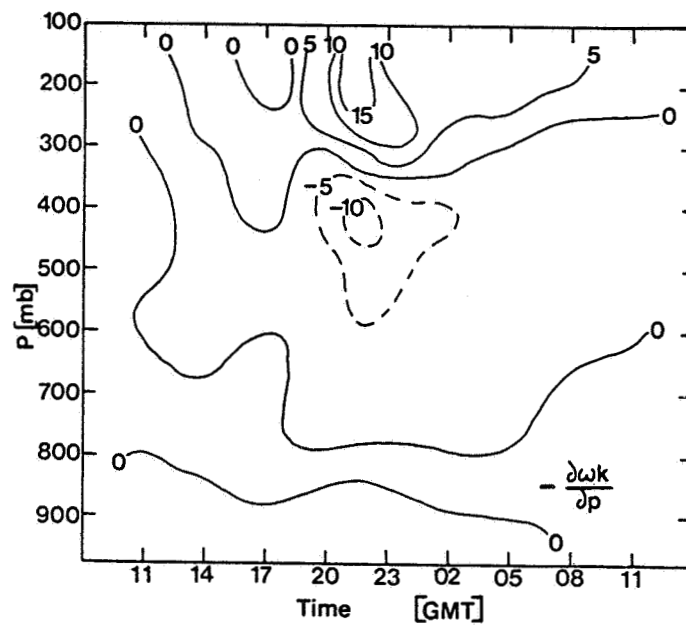
Fig. 15.  Pressure-time cross section of area-averaged vertical
flux divergence of kinetic energy.  Units are
W m$^{-2}$/50 mb.

54

Results of the area-averaged calculations demonstrate that the storm scale environment contains intense energy conversions and transports that are maximized at the time of strongest convection. Table 8 quantifies conditions at 2130 GMT. As noted earlier, the environment is characterized by intense generation and negative dissipation in the upper troposphere. Horizontal outflow is a major upper level energy sink. In addition, present findings indicate that the energy balance is highly variable and fluctuates most rapidly during the times of storm activity. One should note, however, that several of the energy parameters began to change before the onset of the thunderstorms at 1700 GMT. Thus, some changes may be associated with atmospheric processes that helped create an environment suitable for the convection that followed. An additional factor may be diurnal variations in some energy terms (Kung, 1967).

Finally, Fig. 16 shows time fluctuations of surface-150 mb values over Oklahoma that were derived from the concurrent synoptic-scale data network. Except for horizontal flux, patterns of the terms are similar to those derived from mesoscale data (Fig. 10); however, magnitudes from the NWS network are much smaller than those described earlier. The synoptic-scale network failed to capture the strong export of energy from the storm environment. In addition, energy variations associated with the jet intrusion at 0800 GMT are not indicated.

Table 8. Area-averaged energetics of the meso $\beta_2$-scale energy analysis region at 2130 GMT 20 May 1979. Values of K are $10^5$ J m$^{-2}$ while others are W m$^{-2}$.

| Pressure Layer (mb) | K | $\partial K/\partial t$ | $-\vec{V}\cdot\vec{\nabla}\phi$ | $-\vec{\nabla}\cdot k\vec{V}$ | $-\partial\omega k/\partial p$ | D | $-\vec{V}\cdot\vec{\nabla}k$ | $-k(\vec{\nabla}\cdot\vec{V})$ |
|---|---|---|---|---|---|---|---|---|
| 200–150 | 2 35 | -8 22 | 9 73 | -31 31 | 19 08 | -46 12 | -9 30 | -22 01 |
| 300–200 | 4 15 | -19 69 | 91 88 | -72 75 | 27 11 | -65 93 | -35 66 | -37 09 |
| 400–300 | 2 80 | -3 05 | 48 81 | -21 32 | -8 45 | -22 09 | -7 60 | -13 72 |
| 500–400 | 1 19 | 3 15 | 10 03 | 11 26 | -18 35 | -0 17 | 6 97 | 0 29 |
| 600–500 | 0 79 | -0 86 | -0 80 | 7 83 | -10 02 | 2 53 | 2 89 | 4 94 |
| 700–600 | 0 m7 | -0 07 | -0 31 | 4 08 | -6 72 | 2 88 | 1 89 | 2 19 |
| 800–700 | 0 16 | 0 66 | 0 63 | 1 66 | -0 9 | -0 6U | 1 0U | 0 6Z |
| 900–800 | 0 39 | 0 91 | U 88 | 2 93 | 0 23 | -7 13 | 1 11 | 1 8Z |
| SFC–900 | 0 25 | 0 5Z | 3 73 | 2 25 | -1 71 | -3 7m | 0 79 | 1 46 |
| Vertical Total | 12 05 | -26 65 | 208 98 | -95 37 | 0 16 | -140 02 | -37 87 | -57 50 |
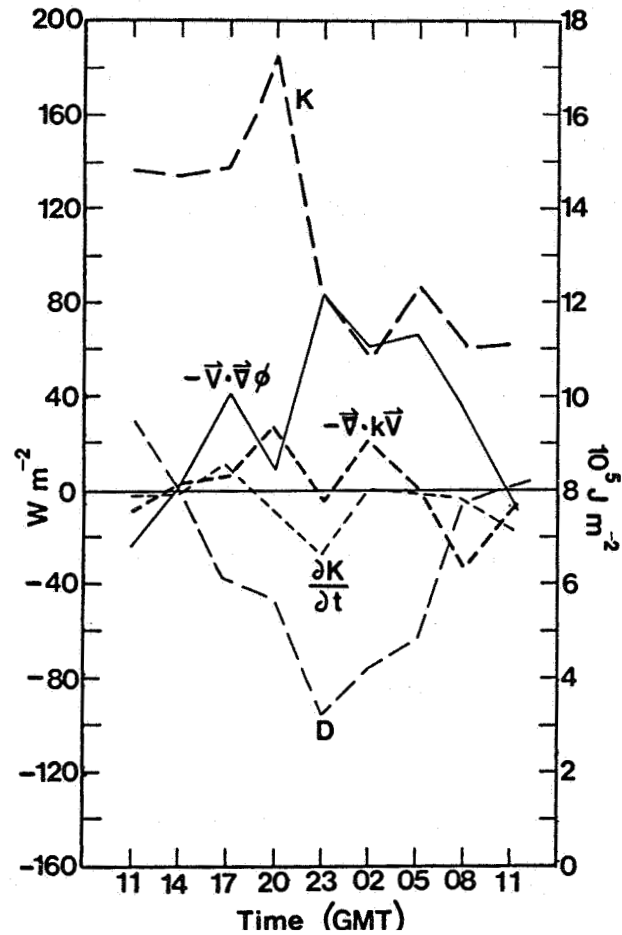
Fig. 16. Time series of synoptic-scale energy budget terms integrated between the surface and 150 mb for the energy analysis region (Fig. 1 ). Three hour time intervals are indicated on the horizontal axis.

## b. Spatial distribution of energy parameters

Horizontal fields of energy terms are presented to describe relationships between environmental wind patterns and various weather phenomena. Integrated kinetic energy content will be shown for all ten observation times, while the budget terms will be presented for two periods of interest. The first period involves energy variations associated with the convection (1700–0200 GMT), while the second concerns jet intrusion from the south near 0800 GMT. All diagrams are for the 400–150 mb layer since this is the region of most intense energetics.

At 1100 GMT, a meso $\beta$ –scale energy maximum is observed over southwestern Oklahoma (Pig, 17). It moves northeastward and by 1400 GMT is located just north of Hinton (HNT), At 300 mb (not shown), winds at Hinton are 48 m $s^{-1}$ compared to 36 m $s^{-1}$ for Clinton Sherman (CSM), situated only 80 km upwind. A significant new'feature at 1700 GMT is the energy decrease in the southeastern corner of the mesonetwork, It is also indicated by the local change term for 1700 GMT (Fig. 18) which, as one should recall, is obtained from centered differences.

Energy content changes dramatically over northwestern Oklahoma between 1700–2000 GMT, coinciding with the period of rapid storm development in the southern portions of the network (Figs. 17–18). Values near Seiling (SEL) increase approximately
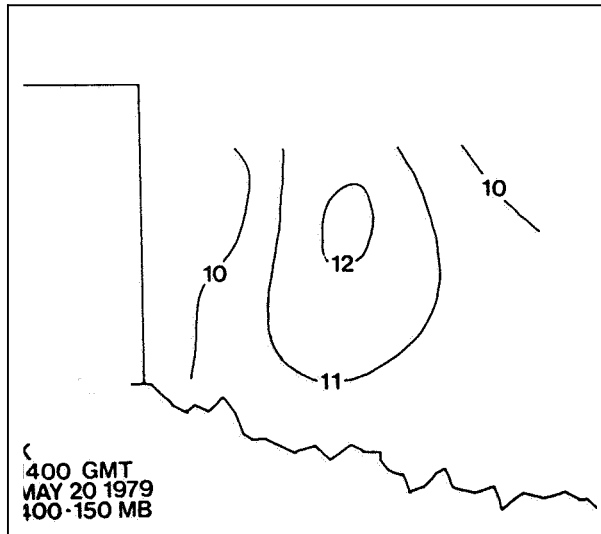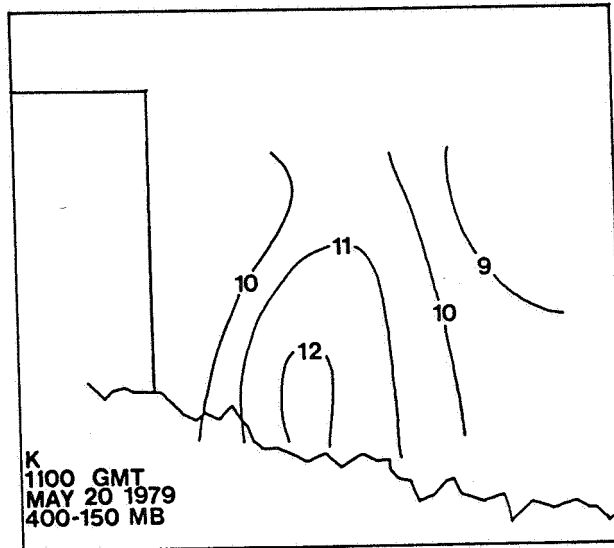
58

a

Fig. 17. Integrated kinetic energy content for the 400–150 mb layer. The dashed line shows the axis for cross sections described in Section 4-c. Units are $10$ J $m^{-2}$.
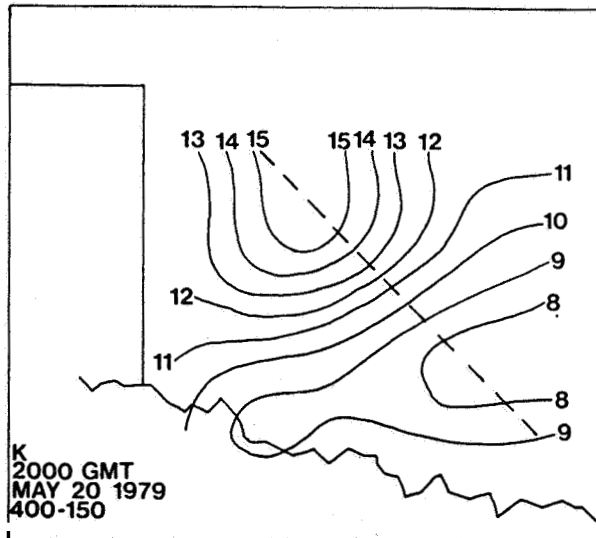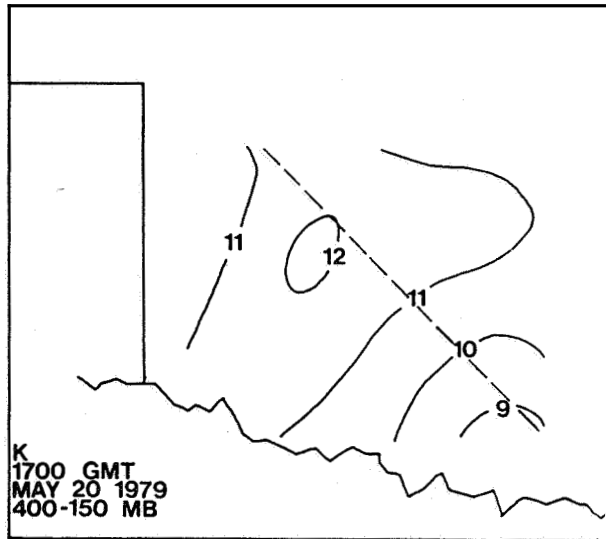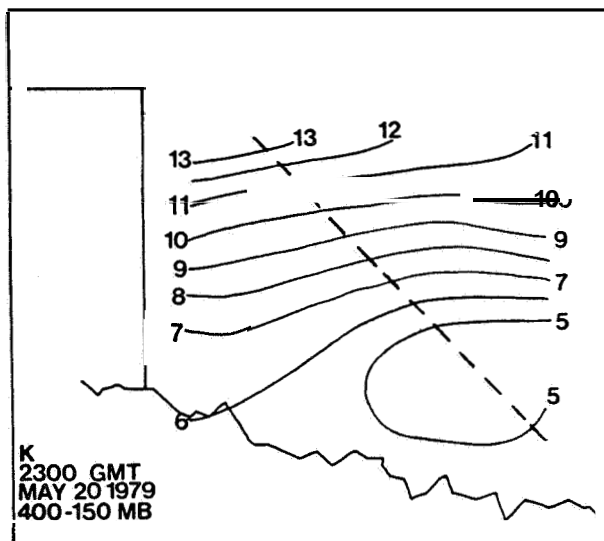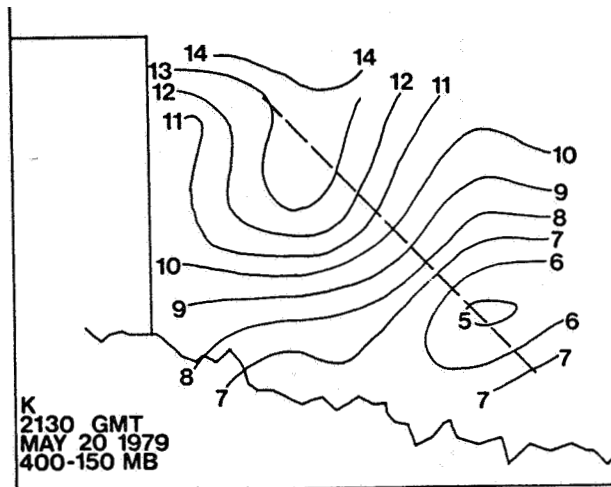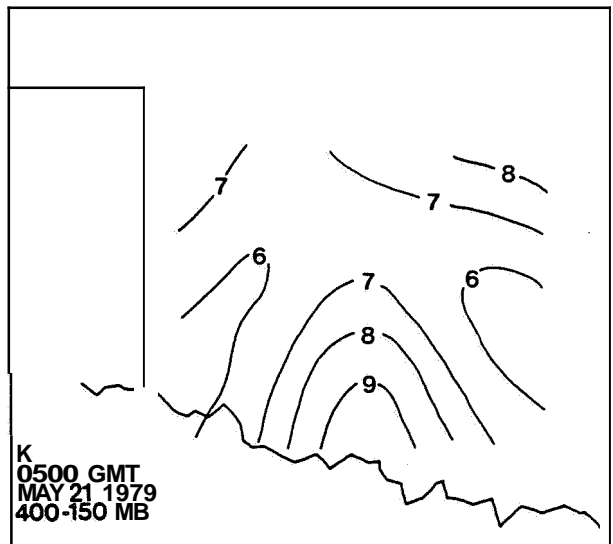
K
1700 GMT
MAY 20 1979
400-150 MB



K
2000 GMT
MAY 20 1979
400-150

Fig. 17.  (continued)

Fig. 17. (continued)

Fig. 17.   (continued)

K
0800 GMT
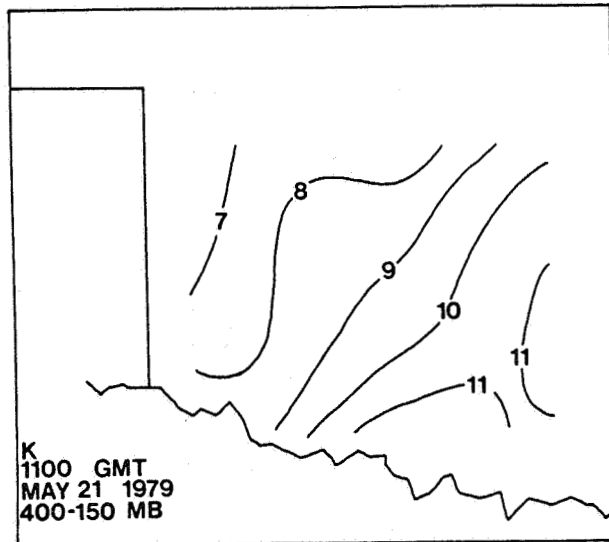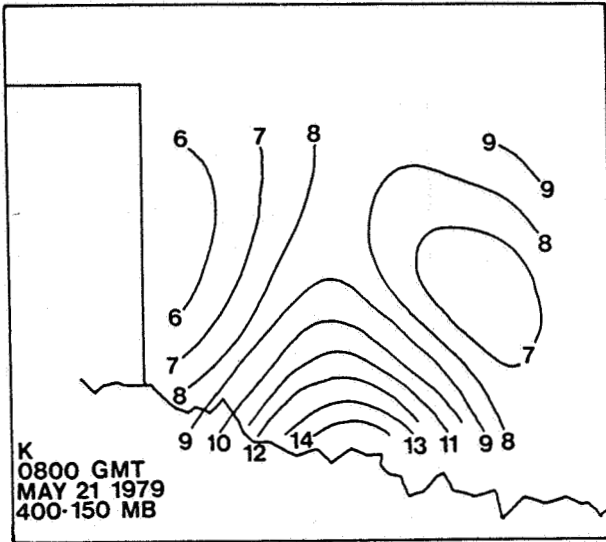MAY 21 1979
400-150 MB

K
1100 GMT
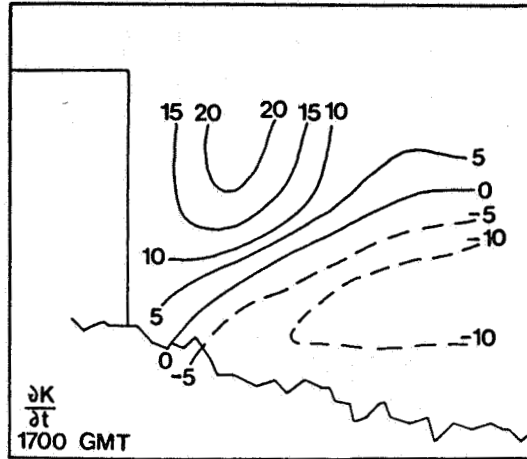MAY 21 1979
400-150 MB

Fig. 17. (continued)

63
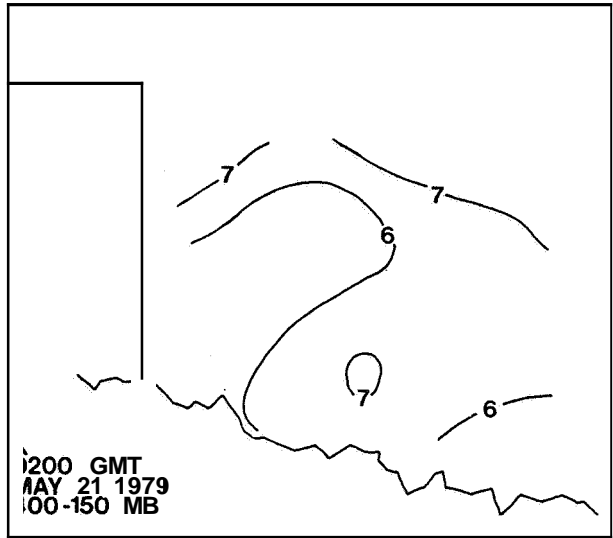
Fig. *18.* Local change of kinetic energy for the *400-150* mb layer. Units are W m$^{-2}$.
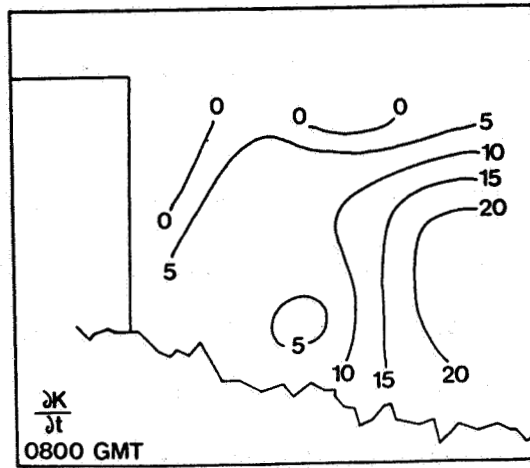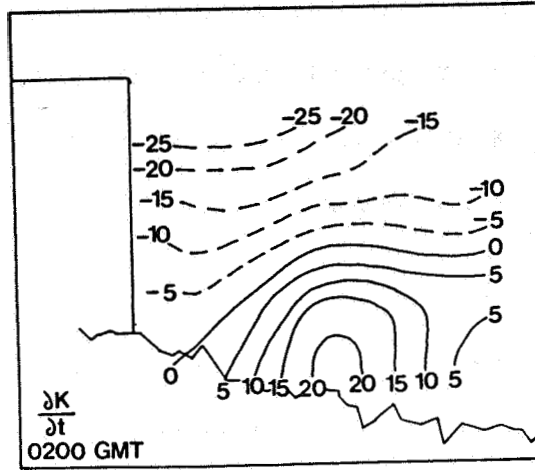
Fig. 18. (continued)

a

40%, producing a localized energy maximum. Greatest values then decrease slightly by 2130 GMT, and by 2300 GMT, the maximum virtually disappears. In contrast, energy content continues to decrease steadily in the southeast. Value, diminish nearly 50% during the 6 h period ending at 2300 GMT. Energy content decreases significantly over most of the mesonetwork by 0200 GMT as the convection weakens.

The timing and locations of the wind/energy variations suggest a relationship with the convective outbreak. Several previous studies have noted the formation of upper level wind maxima on the poleward side of convective complexes (e.g., Fritsch and Maddox, 1981a; Fuelberg and Jedlovec, 1982; Fuelberg and Scoggins, 1978). The current wind maximum in the northwestern corner of the data network also may have been convectively induced. Since mesoscale modelling studies by Fritsch and Maddox (1981b) revealed that a distinct speed maximum had formed after only one hour of simulated convection, the timing of the present case seems quite reasonable. A comparison with energy fields from the surrounding synoptic-scale network at 2000 GMT (Fig. 19) shows that the meso B-scale maximum over northwest Oklahoma may be the southern fringe of a larger jet feature located farther north.

The wind/energy fluctuations in the southeastern part of the network also may be convectively related. However, a somewhat puzzling aspect of AVESESAME V is that these upper level winds began to decrease between 1400-1700 GMT, prior to the onset of
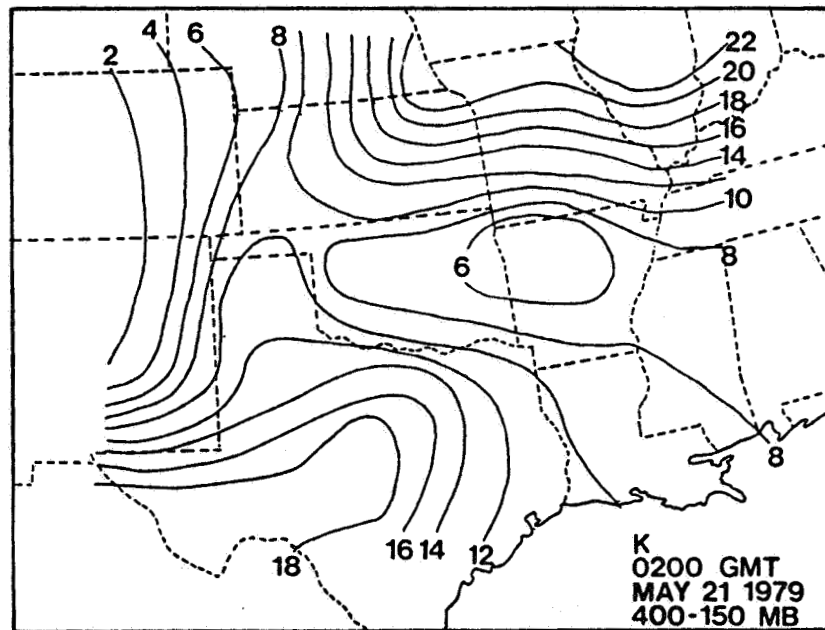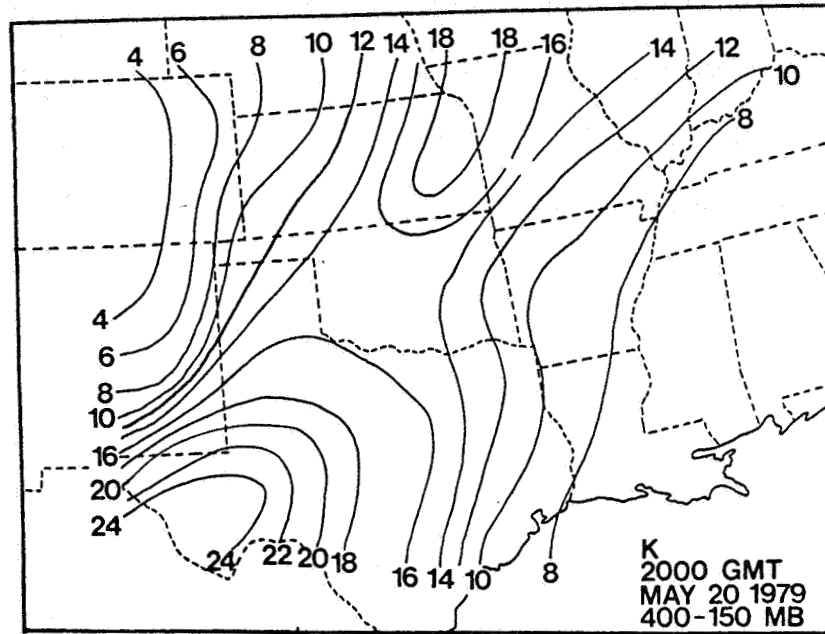
66

Fig. 19.  Integrated kinetic energy content for the 400–150 mb
layer based on the NWS rawinsonde network.  Units are
$10^3$ J m$^{-2}$.

convection.   This implies that storm-environment interactions were not the sole factors producing the wind variability.   In fact, the energy diagram from the synoptic-scale network at 0200 GMT (Fig. 19) reveals that the minimum over southeastern Oklahoma is part of a much larger feature centered over Arkansas.   Nevertheless, those changes occurring after 1700 GMT may have been convectively influenced to some extent.   In addition, Section 4c will describe a vertical wind couplet in this region that appears to be storm induced .

Patterns of the remaining terms now will be described just prior to and during the convective outbreak.   Pronounced changes in cross-contour generation are observed between 1700-0200 GMT (Fig. 20).   At 1700 GMT, maximum generation occurs just east of the Texas panhandle.   Values increase significantly by 2130 GMT when greatest generation is found northeast of the convection. Strongly divergent and ageostrophic flow with large crossing angles (see Fig. 6) produce generation in excess of 300 W $m^{-2}$. Values decrease dramatically by 0200 GMT as the diffluence and mesoridging diminish in response to the weakening convective activity.

Velocity divergence at 1700 GMT (not shown) is relatively weak; therefore, patterns of horizontal flux divergence at this time (Fig. 21) mainly reflect advection of kinetic energy.   A comparison with the corresponding diagram of energy content (Fig. 17) shows that inflow is found downwind (northeast) of energy maxima
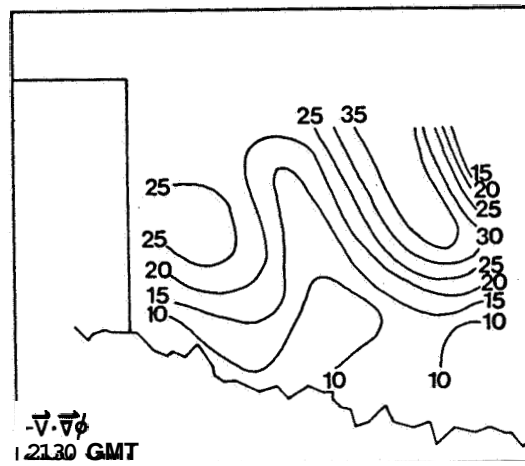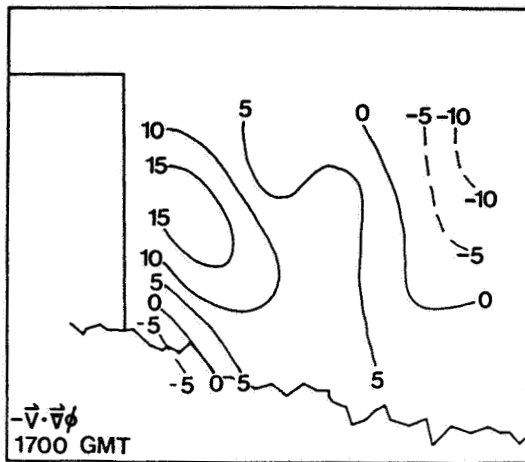
Fig. 20. Cross–contour generation of kinetic energy for the 400–150 mb layer. Units are $10$ W m$^{-2}$.
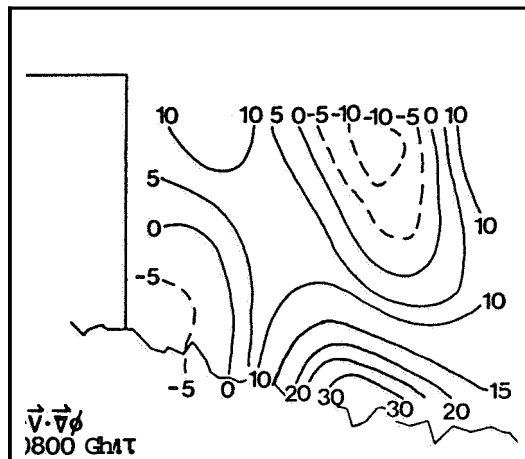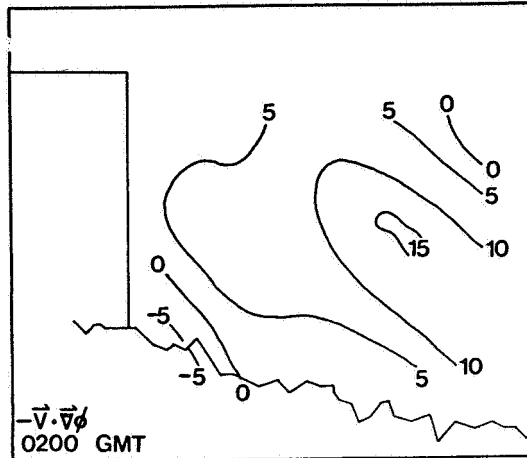
Fig. 20. (continued)
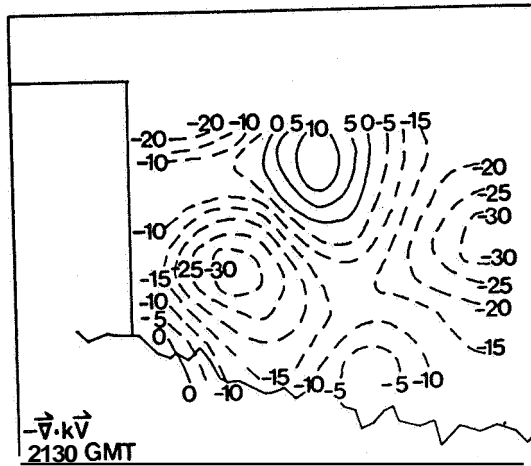
Fig. 21. Horizontal flux divergence of kinetic energy for the 400-150 mb layer. Units are $10^1$ W m$^{-2}$.

$-\vec{\nabla}\cdot k\vec{V}$
0200 GMT



$-\vec{\nabla}\cdot k\vec{V}$
0800 GMT
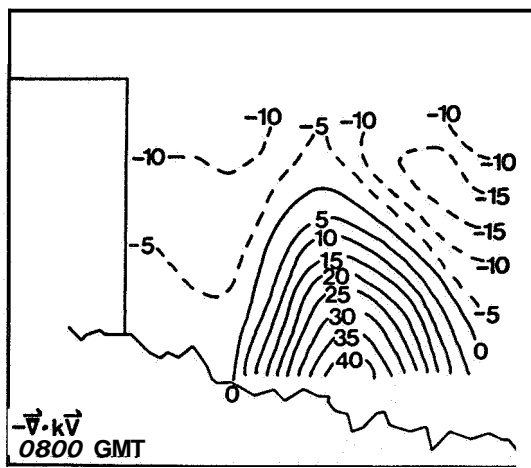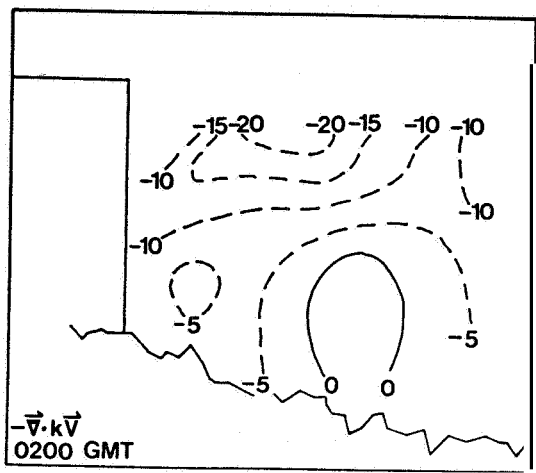
Fig. 21.    (continued)

and vice versa. Flux values strengthen to as much as $-300$ W m$^{-2}$ by 2130 GMT when strong upper level velocity divergence and horizontal advection produce energy export over most of the region. The only exception is the northcentral area of energy import which is attributable to velocity Convergence. Values diminish by 0200 GMT. At 2130 GMT, upward vertical motion reaches $-60$ $\mu$b s$^{-1}$ at 500 mb in the southeastern edge of the region (not shown). This produces large import of energy from the lower levels (Fig. 22). The much weaker vertical export in the northcentral region may be due to compensating downward motion outside the near storm environment .

Finally, fields of dissipation (Fig. 23) show that much of the energy generated within the storm environment is transferred to non-resolvable scales of motion, thereby providing a prominent energy sink to the meso B-scale. At 2130 GMT, however, the southern portion of the network containing the storms has the smallest negative values and, in fact, exhibits a small area of positive dissipation. The primary area of negative values is located farther north, near the region of greatest cross-contour generation (Fig. 20).

A second interesting feature during AVESESAME V is the intrusion of a wind maximum into the special network from 'the south during the final third of the experiment period (Figs. 17-18). The perturbation is first evident at 0500 GMT, and maximum energy content is reached at 0800 GMT when levels had increased
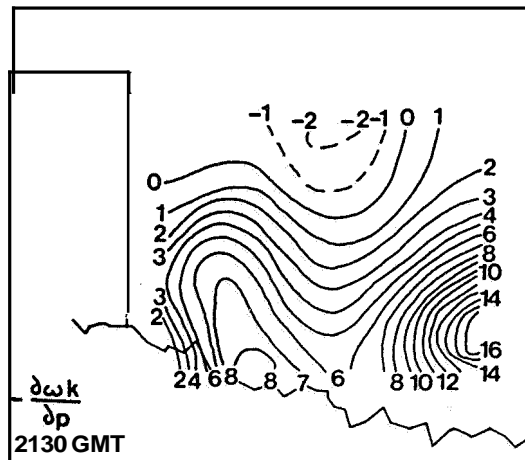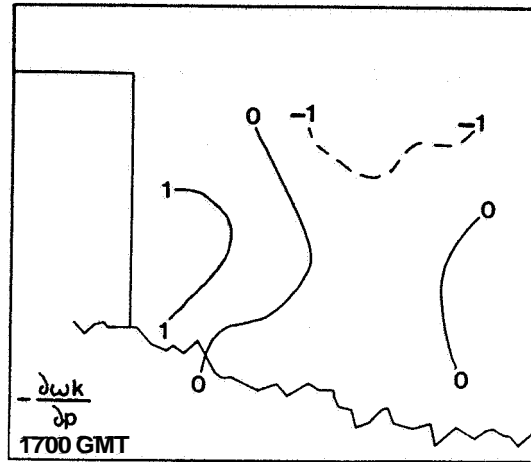
Fig. 22. Vertical flux divergence of kinetic energy for the 400-150 mb layer. Units are $10^1$ W m$^{-2}$.

2 3 4    4 3 2

1

1

$-\dfrac{\partial \omega k}{\partial p}$

0200 GMT

1

1 2            2

1

0

0

1      1

1

0  -1    -1  0  1

$-\dfrac{\partial \omega k}{\partial p}$

0800 GMT
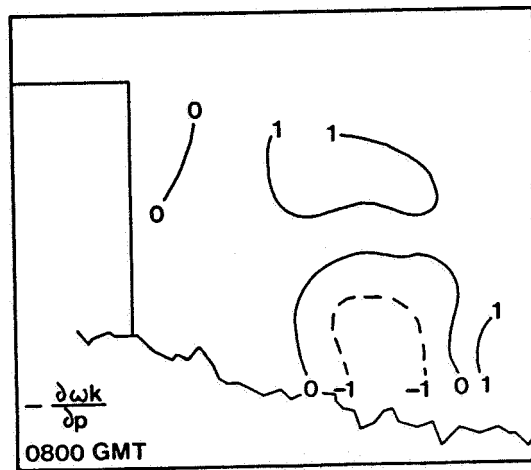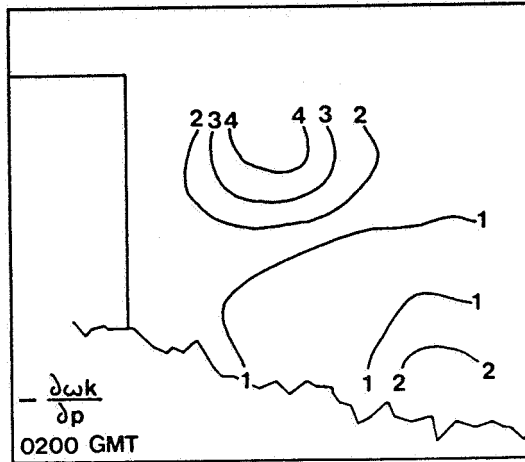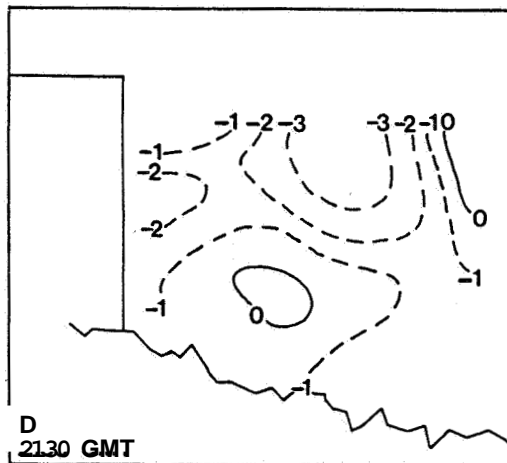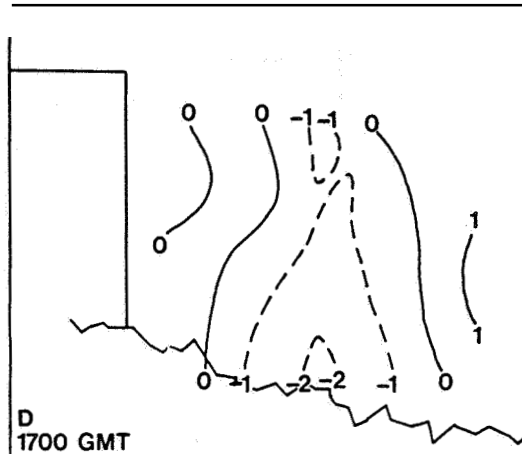
Fig. 22.    (continued)

Fig. 23. Dissipation of kinetic energy for the *400–150* mb layer. Units are $10^2$ W m$^{-2}$.
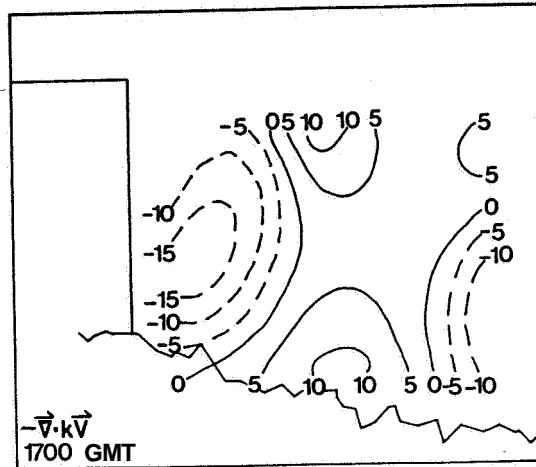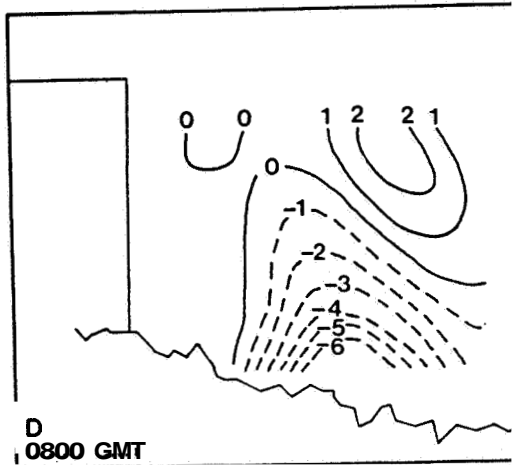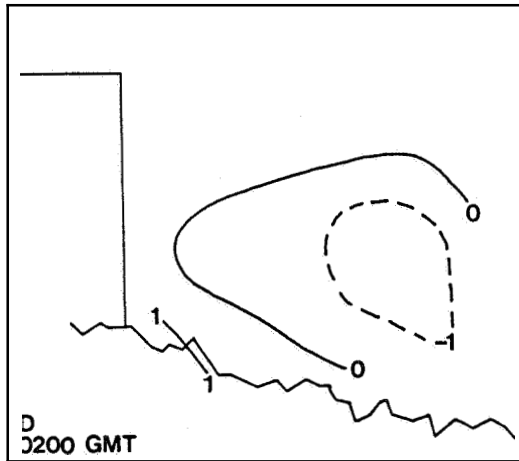
Fig. 23.    (continued)

approximately 50% from those 6 h earlier. By 1100 GMT 21 May, it had weakened and/or moved out of the special network. Mechanisms producing the wind maximum are unknown; however, it may be related to thunderstorm activity in northcentral Texas. The feature was not detected by the NWS stations. Spatial maps for 0800 GMT show the energy balance for the feature, Horizontal flux convergence exceeding 400 W $m^{-2}$ is its greatest energy source (Fig. 21). Calculation of the two flux components (see (2)) indicates that energy import primarily results from advection, and not velocity convergence, Another important energy source to the southcentral region is cross-contour generation (Fig. 20) which reaches 300 W $m^{-2}$. A center of destruction is located downwind of the energy maximum, apparently due to supergradient flow in advance of the feature.

Dissipation due to unresolvable scales of motion that reaches –700 W $m^{-2}$ is the greatest energy sink to the area of the wind maximum (Fig. 23). Farther north of the feature, however, a region of weaker positive dissipation is located near the area of supergradient flow (negative generation). Previous synoptic–scale studies also have noted destruction of kinetic energy and positive dissipation in advance of propagating jet streaks (e.g., Robertson and Smith, 1980). Finally, downward motion provides a small energy sink to the jet area (Fig. 22).

C. Vertical variations in wind

Horizontal maps of kinetic energy content revealed decreases in the southeastern portion of the network between 1400-2300 GMT (Fig. 17). More detailed diagnoses in this section indicate a complex vertical pattern that is superimposed. Cross sections of energy content along an axis from near Seiling (SEL) southeastward to near Elmore City (EMC) are presented in Fig. 24. The axis passes through both the energy maximum and minimum seen earlier (Fig. 17). Greatest energy content at 1700 GMT is located in the northwest, near 250 mb. Between 1700-2000 GMT, upper level values increase near Seiling and Hinton. On the other hand, significant energy decreases occur in the southeast, most notably in the 300-200 mb layer. Energy content then decreases between Seiling and Hinton by 2300 GMT, but a vertical couplet develops in the southeast, where a minimum was observed in the 400-150 mb layer (Fig. 17). Notable energy increases occur near 400 mb while a significant energy decrease is seen near 200 mb. Although most pronounced over the southeastern part of the network, the feature was detected in the area-averaged local change term (Fig. 11), thereby indicating that it is characteristic of a rather large part of the AVE-SESAME V region.

The time series of horizontal wind speed for Healdton (HEA) clearly shows the fluctuations (Fig. 25). Above 300 mb, speeds decrease slowly between 1100-2000 GMT, but then decrease nearly
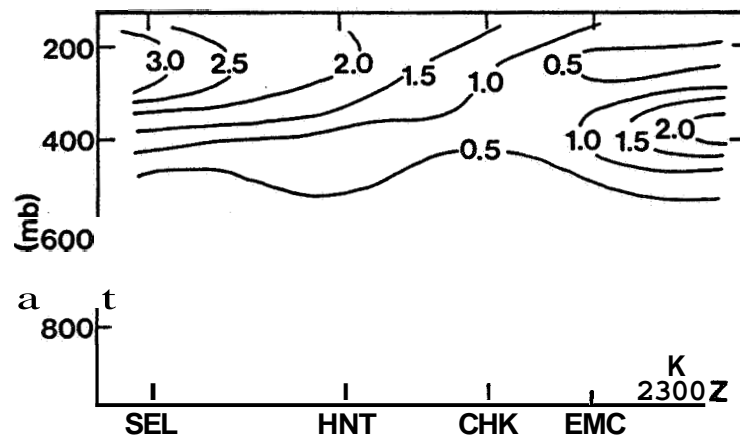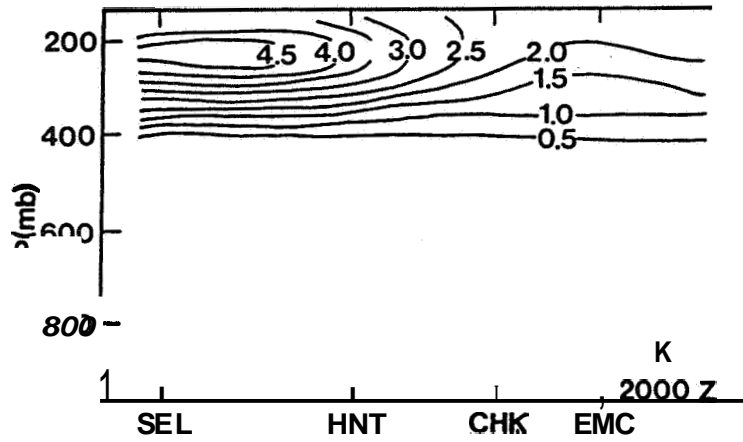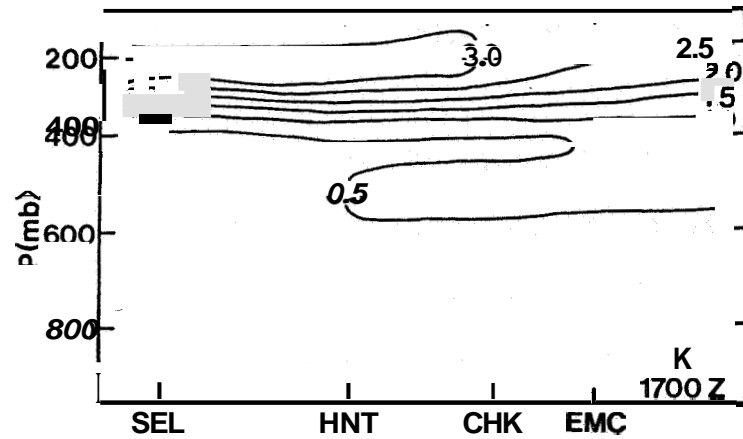
Fig. *24.* Cross sections of kinetic energy content along the **axis shown** in Fig. 17. Units are $10^5$ J m$^{-2}$/50 mb.
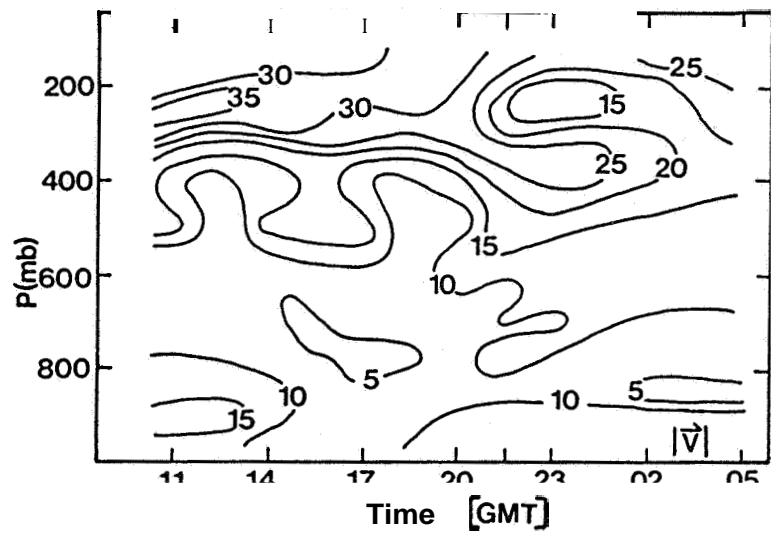
Fig. 25. Times series of horizontal wind speed for Healdton
(HEA). Units are m s$^{-1}$.

50% during the 3 h period between 2000-2300 GMT. On the other hand, values nearly double near 400 mb in the same 3 h period. As a result of the rapid fluctuations, the altitude of maximum wind speed drops approximately 200 mb in only 3 h. By 0500 GMT, the wind patterns return to near original configurations. Similar variations near 2300 GMT also appear in the time series for Chickasha (CHK), Mountain View (MTV), KTW (TVY), Hinton (HNT), Wichita Falls (SPS), Altus (LTS), and Fort Sill (FSI), although they are not as pronounced. These agreements suggest that the changes are valid and not merely attributable to data uncertainties.

The upper level wind variations appear to be related to the nearby convective activity. Similar fluctuations have been documented during AVE-SESAME I which coincided with the Red River Valley tornado outbreak (Vincent and Carney, 1982; Vincent & &., 1981). In that case, a mid-level jet formed near 500 mb during the thunderstorm activity. Upper level winds showed corresponding decreases. When the convection diminished, the mid-level jet also dissipated.

To isolate energetics of the wind couplet from that of the remainder of the analysis region, grid point values of the energy budget were averaged over a fixed subvolume ($1.5 \times 10^4$ km$^2$ area) in which the feature was most pronounced (Fig. 1). The pressure-time cross section of the local change term (Fig. 26) shows that the couplet occurs between 2000-2300 GMT. Energy decreases are

82

d
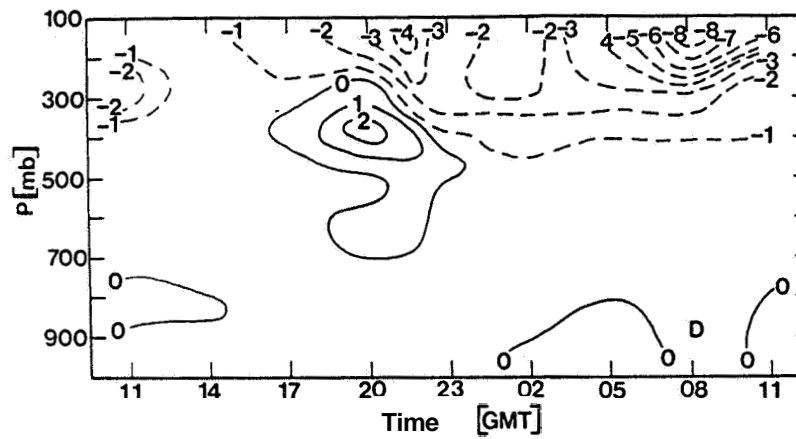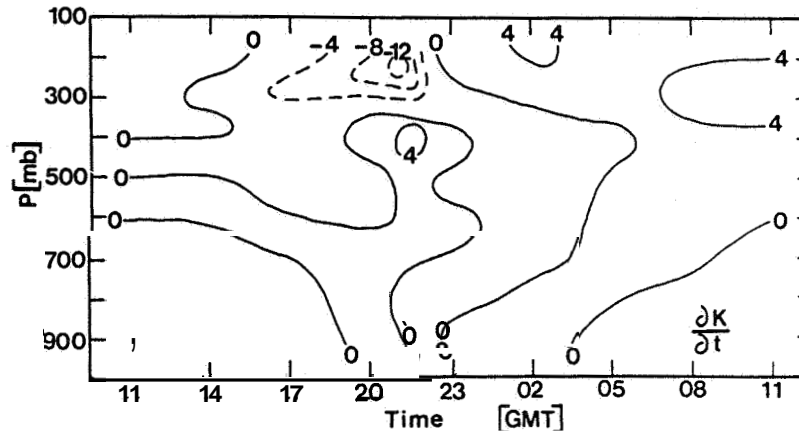
Fig. 26.  Pressure-time cross sections of energy budget terms
averaged over the subvolume in Fig. 1.  Units are
$10^1$ W m$^{-2}$/50 mb, except for $\partial K/\partial t$ which is W m$^{-2}$/
50 mb.

83
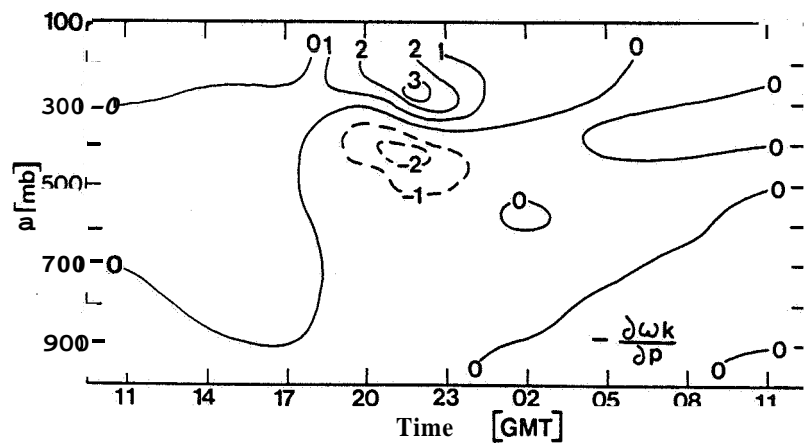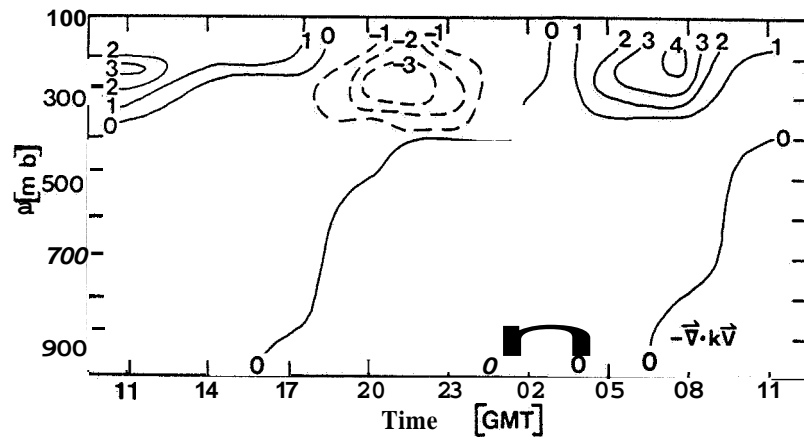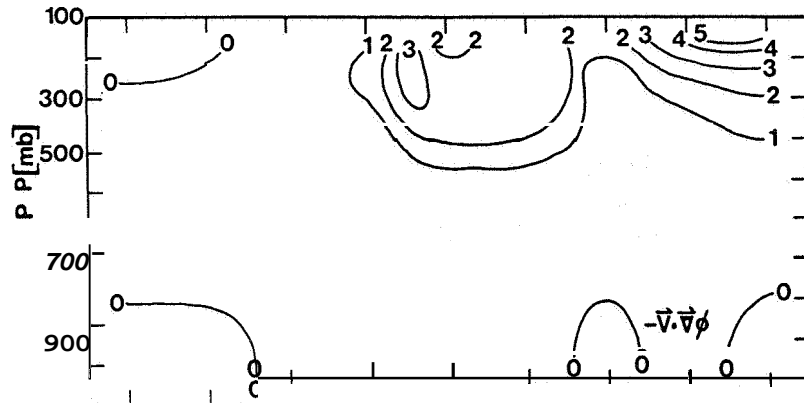
Fig. 26. (continued)

found in the 350-150 mb layer, whereas greatest increases occur between 550-350 mb. Table 9 presents integrated totals of the energy budget for both of these layers.

Energy content within the 350-150 mb layer decreases significantly during the 3 h period of intense storm activity. The original value of 7.63 x $10^5$ J $m^{-2}$ at 2000 GMT drops nearly 50% to 3.95 x $10^5$ J $m^{-2}$ at 2300 GMT. Table 9 and Fig. 26 indicate the energy mechanisms producing the vertical couplet. With the exception of large values near 0800 GMT which are due to the jet intrusion described earlier, greatest magnitudes occur near 2130 GMT. This finding is similar to that observed for the entire analysis area (Fig. 10). At 2130 GMT, generation and vertical flux convergence provide sources to the 350-150 mb layer that are 136.50 W $m^{-2}$ and 95.90 W $m^{-2}$, respectively. However, energy sinks by horizontal outflow (-130.45 W $m^{-2}$) and negative dissipation (-136.00 W $m^{-2}$) override to produce an overall energy decrease. The relative contributions of the four budget terms are similar at all three times of intense convection (Table 9).

Contrary to findings of the topmost layer, energy content between 550-350 mb increases during the same 3 h period (Table 9, Fig. 26). At 2000 and 2130 GMT, significant sinks by vertical flux divergence and weaker sinks by horizontal export are counteracted by sources due to generation and positive dissipation. It is noteworthy that at 2000 GMT, energy transfer from non-resolvable scales (33.15 W $m^{-2}$) is an even greater source than

85

Table 9. Integrated energy values for two layers of the subvolume enclosing the vertical wind couplet (see Fig. 1). Values of K are $10^5$ J m$^{-2}$ while others are W m$^{-2}$.

| Pressure Layer (mb) | K | $\partial K/\partial t$ | $-\vec{V}\cdot\vec{\nabla}\phi$ | $-\vec{V}\cdot k\vec{V}$ | $-\partial\omega k/\partial p$ | D |
|---|---|---|---|---|---|---|
| **2000 GMT** | | | | | | |
| 350–150 | 7.63 | -23.56 | 38.63 | -93.18 | 45.56 | -14.57 |
| 550–350 | 1.75 | 0.87 | 5.69 | -5.87 | -32.10 | 33.15 |
| **2130 GMT** | | | | | | |
| 350–150 | 5.46 | -34.08 | 130.50 | -130.45 | 85.90 | -136.00 |
| 550–350 | 2.59 | 10.6a | 38.68 | -1.62 | -06.57 | 38.97 |
| **2300 GMT** | | | | | | |
| 350–150 | 3.95 | -0.96 | 97.18 | -90.90 | 67.34 | -74.58 |
| 550–350 | 2.87 | 0.03 | 55.06 | 8.72 | -49.88 | -13.87 |

86

that due to cross-contour flow (5.69 W $m^{-2}$). At 2130 GMT, positive dissipation is only slightly smaller than generation. The energy balance changes somewhat by 2300 GMT when generation and horizontal import are in near balance with negative dissipation and vertical flux divergence.

Results indicate that the complex vertical fluctuations of wind (energy) are due to differing balances between the various budget terms. The importance of positive dissipation is especially significant. Since dissipation is computed as a residual, its uncertainty is somewhat greater than that of the other terms. Nonetheless, sensitivity analyses demonstrate that errors are not its dominant component (e.g., Appendix, Ward and Smith, 1976; Fuelberg and Jedlovec, 1982). Large magnitudes of dissipation at times of greatest convective activity (2000-2300 GMT) suggest that the near storm environment is highly influenced by motions which are not adequately resolved by the meso $\beta$-scale data network. One possible explanation is that meso y-scale vertical motions within the deep convection are "mixing" the air, thereby producing a sink at the original jet level and a corresponding source at levels below. This effect would not be measured by the other budget terms which describe meso $\beta$-scale mechanisms. In a somewhat similar manner, Vincent and Schlatter (1979) noted that subgrid scale processes were an energy supply to the 500-300 mb synoptic-scale flow during times of intense convection. They speculated that potential energy on the cumulus scale was transferred to kinetic energy on the synoptic scale,

5. SUMMARY AND CONCLUSIONS

A meso 8-scale kinetic energy analysis was conducted for a period of intense thunderstorm activity that occurred over central Oklahoma during AVE–SESAME V (20–21 May 1979). Rawinsonde data at 75 km spacings at either 3 or 1.5 h intervals were used to examine energy processes of the mesoscale storm environment prior to, during, and after peak convection. The goal was to better understand how areas of storms modify their surrounding larger scale environment. Unlike previous meso 8-scale energy studies which emphasized a collection of days, the current investigation was a detailed analysis of a single 24 h period.

Area-averaged energetics indicated that the meso β-scale storm environment was characterized by generation of kinetic energy by cross-contour flow, horizontal flux divergence of energy, upward transport by ascending motion, and transfer of energy from resolvable to non-resolvable scales of motion (negative dissipation). Vertical profiles showed that processes were greatest near jet stream level.

Current results were compared with previous studies by Tsui and Kung (1977) (T & K) who computed energy budgets for nine days using meso 8-scale NSSL data. Findings of AVESESAME V were very similar to those from T & K's composite convective group. Both were characterized by strong generation and significant energy

88

losses by negative dissipation. Although horizontal flux diver-
gence was a major energy sink during AVE–SESAME V, this was not
the case in T & K's investigation. Differing locations of wind
maxima between the two studies may have contributed to this con-
trast.

A unique feature of AVE-SESAME V is that rawinsonde data were
simultaneously collected at both the synoptic and meso @-scales.
Therefore, a comparison of the kinetic energy balance of the same
analysis region based upon different scales of input data received
special attention. To the authors' knowledge, such a comparison
has never previously been reported in the literature. The ener-
getics of the two resolutions was similar in that generation and
dissipation dominated both the mesoscale storm environment and the
synoptic–scale flow. However, magnitudes were larger at the finer
resolution. The coarser network failed to detect the enhanced
horizontal flux divergence within the storm environment.

The meso $\beta$-scale energy budget underwent major time fluctua-
tions. Pressure–time cross sections showed that maximum variabil-
ity occurred above 400 mb, centered about the time of greatest
storm activity. Strong upper level generation during the convec-
tive outbreak was attributable to storm–induced divergent flow
being superimposed on a mesoridge. Magnitudes and variability of
horizontal flux divergence and dissipation were very similar to
those of generation, thereby indicating that much of the kinetic
energy generated in the mesoscale storm environment was exported

outside the region and transferred to non-resolvable scales of motion. Except for horizontal flux, time variability of energy parameters derived from synoptic-scale data was similar to that from the special network.

Horizontal fields of energy content **for** the 400–150 mb layer were presented to describe flow patterns of the meso 6-scale storm environment. Energy content was seen to change dramatically during the period of intense convection. Winds strengthed abruptly north of the convective area as the severe thunderstorms developed. Corresponding values of energy content increased approximately 40% in only 3 h. These findings agree with those of jet development poleward of Mesoscale Convective Complexes. In contrast. energy content southeast of the storms decreased slowly prior to the convective outbreak, but then diminished as much as 50% once the convection developed. In addition, the horizontal maps showed the intrusion of a wind maximum into the region from the south during the latter part of the experiment period. Energy levels in that area increased approximately 50% during a 6 h period.

Horizontal maps of the energy budget parameters showed good agreement with observed weather features. During the times of intense convection, strong cross-contour flow produced large generation north of the storm area. Fields of dissipation indicated pronounced transfers of energy to non-resolvable scales over most of the region. Negative centers were co-located with areas of

maximum generation. Interestingly, however, at the time of peak storm intensity, a small area of positive dissipation existed near the convection. Strong horizontal flux divergence was an energy sink over most of the region, whereas vertical flux convergence was a major source. The area of jet intrusion toward the end of the period was characterized by horizontal flux convergence. cross-contour generation, and negative dissipation,

Finally, detailed diagnoses at the time of peak convection revealed a complex vertical pattern of wind variations above 600 mb in the southeastern part of the network. The feature was super-imposed on generally decreasing winds that began prior to the storm outbreak. Speeds near 200 mb decreased approximately 50% during the 3 h period coinciding with the most active storms. On the other hand, winds near 400 mb nearly doubled during the same 3 h period. As a result, the level of maximum speeds dropped approximately 200 mb. To explain this feature, a kinetic energy analysis was conducted for a subvolume of the total analysis region to isolate the speed variations. Results indicated that the vertical fluctuations of wind (energy) were due to differing balances among the various energy budget terms. Large magnitudes of dissipation suggested that the mesoscale storm environment was highly influenced by motions that were not adequately resolved by the meso $\beta$-scale network. Vertical variations in dissipation con-tributed greatly to the vertical variation of wind.

Energy/wind relations during AVE–SESAME V appear consistent

91

with those of previous storm-environment studies. However, AVE-SESAME V is a singularly well documented case. We hypothesize that the thunderstorms produced many of the observed energy variations. Scale interactions appear extremely complex in the near storm environment. Unfortunately, our understandihg of sub-synoptic phenomena, as well as scale interactions, is very limited. Thus, many more theoretical, diagnostic, and numerical investigations are needed to explain the observed phenomena. As our overall knowledge of the smaller scales improves, greater forecasting skill will result.

a

APPENDIX

## Sensitivity Analysis

The purpose of the sensitivity analysis is to quantify the effects of random errors in the rawinsonde data on the kinetic energy budget parameters. Our procedure was to add computer generated random perturbations that simulated actual rawinsonde errors to the original time adjusted 25 mb data at individual stations. Then, energy budgets were calculated from the perturbed data and compared with those derived from the original data. The sensitivity is represented by mean absolute differences and mean correlation coefficients between the original and perturbed budgets. This technique is similar to that used previously by Ward and Smith (1976), Robertson and Smith (1980), and Fuelberg and Jedlovec (1982).

Perturbations introduced into the original data were normally distributed about zero with standard deviations as a function of pressure (Table 10). Deviations for levels not shown can be obtained by linear interpolation. The values are similar to those suggested by Fuelberg and Jedlovec (1982). Because of the care taken in processing and checking the data, perturbations were restricted to two standard deviations from zero which included about 95 % of the possible values.

Since maximum convective activity and strongest energetics

Table 10.  Standard deviations of perturbations normally distributed about zero.

| Pressure level (mb) | Wind direction (deg) | Wind speed (m s$^{-1}$) | Height (m) |
|---|---|---|---|
| 150 | 10.0 | 4.3 | 32.0 |
| 200 | 9.1 | 4.0 | 28.0 |
| 300 | 7.0 | 3.7 | 21.0 |
| 500 | 4.6 | 3.0 | 11.0 |
| 700 | 3.5 | 2.0 | 8.0 |
| 900 | 2.0 | 1.0 | 4.1 |

occurred near 2130 GMT 20 May, this observation time was chosen for the analysis. Ten versions of the data, each with a different set of perturbations, were made for 2130 GMT. Analytical procedures (Barnes analysis, vertical motions, etc.) used with the perturbed data were identical to those used with the original data (see Sections 2c and 2d). By comparing the original and perturbed data grids, it was found that approximately 35 % of the magnitudes of height perturbations introduced at the station locations (Table 10) were removed by the Barnes analysis scheme. Since winds were vertically filtered before the objective analysis, approximately 55 % of their introduced error was removed. Thus, our computational procedures have the desired ability to reduce the inherent error within the data set,

Original budget values along with mean absolute differences and correlation coefficients between original and perturbed versions are given in Table 11 for the entire energy averaging region and in Table 12 for the limited area in the southeast (see Fig.1). Results show that the dissipation and generation terms are most sensitive to random error. The greater uncertainty in dissipation is expected since it is computed as a residual from the other budget terms (see (1)). McInnis and Kung (1972) have commented on the difficulties in accurately calculating the generation term. On the other hand, terms representing energy content and vertical and horizontal flux divergence appear to be the most reliable. With the exceptions of dissipation for the 700-400 mb layer over

95

Table 11  Area-averaged kinetic energy budget for 2130 GMT 20 May 1979.  Values in parentheses are mean absolute differences between the original and ten perturbed budgets.  Values in brackets are mean correlation coefficients.  The budget area consists of the overall energy analysis region shown in Fig. 1.  All units of energy parameters are W m$^{-2}$, except for K which is $10^5$ J m$^{-2}$.

| Pressure Layer (mb) | K | $\partial K/\partial t$ | $-\vec{V}\cdot\vec{\nabla}\phi$ | $-\vec{V}\cdot k\vec{\nabla}V$ | $-\partial\omega k/\partial p$ | D |
|---|---|---|---|---|---|---|
| 400–150 | 9.30 [0.99] (0.24) | -30.96 [0.98] (0.75) | 190.42 [0.82] (24.57) | -125.38 [0.96] (6.82) | 38.14 [0.99] (2.14) | -134.14 [0.87] (26.02) |
| 700–400 | 2.35 [0.99] (0.0?) | 2.22 [0.99] (0.35) | 9.32 [0.80] (4.28) | 23.17 [0.98] (2.41) | -35.51 [0.99] (2.10) | 5.24 [0.87] (5.91) |
| Sfc–700 | 0.80 [0.99] (0.02) | 2.09 [0.99] (0.11) | 9.24 [0.92] (1.24) | 6.84 [0.98] (0.21) | -2.47 [0.99] (0.22) | -11.52 [0.94] (1.24) |
| Vertical Total | 12.45 [0.99] (0.27) | -26.65 [0.97] (0.82) | 208.98 [0.82] (25.46) | -95.37 [0.95] (7.92) | 0.16 [0.99] (0.00) | -140.42 [0.88] (26.83) |

Table 12. Integrated energy values for two layers of the subvolume enclosing the vertical wind couplet at 2130 GMT (see Fig. 1). Values in parenthesis are mean absolute differences between the original and ten perturbed budgets. Values in brackets are mean correlation coefficients. All units of energy parameters are W m$^{-2}$, except for K which is $10^5$ J m$^{-2}$.

| Pressure Layer (mb) | K | $\partial K/\partial t$ | $-\vec{V}\cdot\vec{\nabla}\phi$ | $-\vec{V}\cdot k\vec{V}$ | $-\partial\omega k/\partial p$ | D |
|---|---|---|---|---|---|---|
| 350–150 | 5.46 [0.97] (....) | -34.05 [0.95] (0 90) | 136.50 [0.86] (17.14) | -130.45 [0.97] (12.79) | 95.90 [0.99] (8.15) | -136.00 [0.77] (18.45) |
| 550–350 | 2.59 [0.99] (0.13) | 10.46 [0.99] (0.45) | 39.68 [0.83] (12.23) | -1.62 [0.90] (3.35) | -66.57 [0.98] (6.51) | B8 97 [0. 5] <1B 0) |

the analysis area, and horizontal flux for the 550-350 mb layer over the limited area, percentages of mean absolute differences to original budget values are less than 35 % (not shown). At any particular level, one can have greater confidence in terms having large magnitudes than those near zero.

To quantify the sensitivity of the horizontal energy patterns, linear correlation coefficients were calculated between grid points of the original field and each of the ten perturbed runs. Results of these calculations also are given in Tables 11 and 12. With the exceptions of the generation and dissipation terms, mean coefficients for the ten runs are never less than 0.90 for either area. For the limited region, the dissipation term of the 350-150 mb layer has the lowest mean correlation (0.77); whereas for the entire region, the generation term has the lowest correlation (0.80) in the *700-400* mb layer. One should note that the dissipation term has a high correlation (0.95) in the 550-350 mb layer of the limited area. This is the layer where subgrid-scale energy transfers were a significant energy source.

Horizontal fields having the lowest correlations of the ten perturbed runs are given in Fig. 27 for generation, horizontal flux, and dissipation of energy, respectively. Original fields of these terms are given in Figs. 20, 21, and 23. Generally, patterns of the worst perturbed fields show good agreements with their corresponding originals. Patterns are nearly identical for horizontal flux divergence, but somewhat greater discrepancies can

98
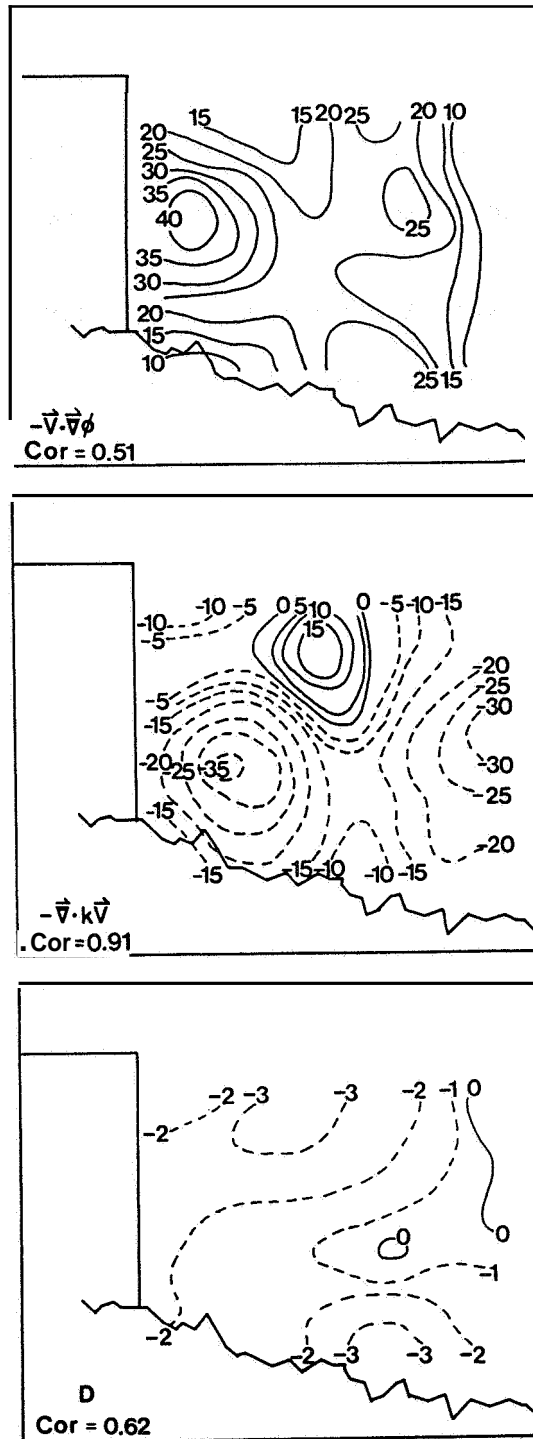
Fig. 27. Horizontal maps of the most perturbed fields for
the 400–150 mb layer at 2130 GMT 20 May. Units
are $10^1$ W m$^{-2}$ for generation and horizontal flux
divergence but $10^2$ W m$^{-2}$ for dissipation.

99

be seen for the other terms. Although data errors sometimes pro-
duces considerable variations at individual grid points, horizon-
tal patterns usually contain the same major features.

In summary, results of the sensitivity analysis show that
random errors in rawinsonde data generally should not affect the
interpretations of the current study. In addition, good space and
time continuities of the original patterns give additional confi-
dence in final results.

# REFERENCES

Alberty, R. L., D. W. Burgess, C. E. Hane, and J. F. Weaver, 1979: SESAME 1979 operations summary. NOAA/ERL, Boulder, CO, 253 pp, (Available from NOAA/ERL, RX8, 325 Broadway, CO 80303.)

Anthes, R. A., Y. -H. Kuo, S. G. Benjamin, and Y. -F. Li, 1982: The evolution of the mesoscale environment of severe local storms: Preliminary modelling results. Mon. Wea. Rev., 110, 1187-1213.

Aubert, E. J., 1957: On the release of latent heat as a factor in large-scale atmospheric motions. J. Meteor., 14, 527-542.

Barnes, S. L., 1964: A technique for maximizing detail in numerical map analysis. J. Appl. Meteor., 3, 396-409.

_____, 1981: SESAME 1979 data user's guide. NOAA/ERL, Boulder, CO, 236 pp, (Available from NOAA/ERL, RX8, 325 Broadway, Boulder, CO 80303.)

Fankhauser, J. C., 1969: Convective processes resolved by a mesoscale rawinsonde network. J. Appl. Meteor., 8, 778-798.

_____, 1971: Thunderstorm-environment interactions determined from aircraft and radar observations. Mon. Wea. Rev., 99, 171-197.

_____, 1974: The derivation of consistent fields of wind and geopotential height from mesoscale rawinsonde data. J. Appl. Meteor., 13, 637-646.

Fritsch, J. M, and R. A. Maddox, 1980: Analysis of upper tropospheric wind perturbations associated with midlatitude mesoscale convective complexes. Preprints Eighth Conf. on Weather Forecasting and Analysis, Denver, 339-349.

_____, and _____, 1981a: Convectively driven mesoscale weather systems aloft. Part I: Observations. J. Appl. Meteor., 20, 9-19.

101

_____, and _____, 1981b: Convectively driven meso-scale weather systems aloft. Part 11: Numerical simulations. J. Appl. Meteor., 20, 20-26.

Fuelberg, H. E, 1974: Reduction and error analysis of the AVE II pilot experiment data, NASA CR-120496, Marshall Space Flight Center, AL, 131 pp. (Available from Atmospheric Sciences Division, ES-84, Marshall Space Flight Center, AL, 35812.)

_____, E, M. Berecek, D. M. Ebel, and G. J. Jedlovec, 1980: Kinetic energy budgets in areas of intense convection. NASA CR-3336, Marshall Space Flight Center, AL, 173 pp. (Available from Atmospheric Sciences Division, ES-84, Marshall Space Flight Center, AL, 35812.)

_____, and G. J. Jedlovec, 1982: A subsynoptic-scale kinetic analysis of the Red River Valley tornado outbreak (AVE-SESAME I). Mon. Wea. Rev., 110, 2005-2029.

_____, and M. F, Printy, 1983: Meso β-scale thunderstorm-environment interactions during AVE-SESAME V (20-21 May 1979). Submitted to Bull. Amer, Meteor. Soc.

_____, and J, R. Scoggins, 1978: Kinetic energy budgets during the life cycle of intense convective activity. Mon. Wea. Rev., 106, 637-653.

Hill, K., G. S, Wilson, and R. E. Turner, 1979: NASA's participation in the AVE-SESAME '79 program. Bull. Amer. Meteor. Soc., 60, 1323-1329.

July, M, J., and R. E. Turner, 1979: A preliminary look at AVE-SESAME V conducted on 20-21 May 1979. NASA TM-82416, Marshall Space Flight Center, AL, 56 pp. (Available from Atmospheric Sciences Division, ES-84, Marshall Space Flight Center, AL, 35812.)

Kung, E C., 1967: Diurnal and long-term variations of kinetic energy generation and dissipation for a five year period. Mon. Wea. Rev., 95, 593-606.

a

_____, and T. L. Tsui, 1975: Subsynoptic-scale kinetic energy balance in the storm area. *J. Atmos. Sci.*, 32, 729-740.

Maddox, R. A., 1980: Mesoscale convective complexes. *Bull. Amer. Meteor. Soc.*, 61, 1374-1387.

_____, D. J. Perkey, and J. M. Fritsch, 1980: The evolution of upper-tropospheric features during the development of a midlatitude. mesoscale convective complex. Preprints Eighth Conf. on Weather Forecasting and Analysis, Denver, 233-239.

McInnis, D. H., and E. C. Kung, 1972: A study of subsynoptic-scale energy transformations. *Mon. Wea. Rev.*, 100, 126-132.

Moore, J. T., and H. E. Fuelberg, 1981: A subsynoptic-scale analysis of the first AVE-SESAME '79 period. *Bull. Amer. Soc.*, 62, 1577-1590.

Ninomiya, K., 1971: Mesoscale modification of synoptic situations from thunderstorms as revealed by ATS III and aerological data. *J. Appl. Meteor.*, 10, 1103-1121.

O'Brien, J. J., 1970: Alternate solution to the classical vertical velocity problem. *J. Appl. Meteor.*, 9, 193-203.

Ogura, Y., and Y. Chen, 1977: A life history of an intense mesoscale convective storm in Oklahoma. *J. Atmos. Sci.*, 34, 1458-1476.

_____, and M. T. Liou, 1980: The structure of a midlatitude squall line: A case study. *J. Atmos. Sci.*, 37, 553-567.

Park, S. -U., and D. N. Sikdar, 1982: Evolution of the dynamics and thermodynamics of a mesoscale convective system: A case study. *Mon. Wea. Rev.*, 110, 1024-1040.

Robertson, F. R., and P. J. Smith, 1980: The kinetic energy budgets of two severe storm producing extratropical cyclones. *Mon. Wea. Rev.*, 108, 127-143.

Sanders, F., and K. A. Emanuel, 1977: The momentum budget and temporal evolution of a mesoscale convective system, J. Atmos. Sci., 34, 322-330.

_____, and R. J. Paine, 1975: The structure and thermo-dynamics of an intense mesoscale convective storm in Oklahoma. J. Atmos. Sci., 32, 1563-1579.

Shuman, F. G., 1957: Numerical methods in weather prediction: II. Smoothing and filtering. Mon. Wea. Rev., 85, 357-361.

Sienkiewicz, M. E., L. P. Gilchrist, and R. E. Turner, 1981: AVE-SESAME V: 25-mb sounding data. NASA TM-82417, Marshall Space Flight Center, AL, 413 pp. (Available from Atmospheric Sciences Division, ES-84, Marshall Space Flight Center, AL 35812).

Tsui, T. L., and E. C. Kung, 1977: Subsynoptic-scale energy transformations in various severe storm situations. J. Atmos. Sci., 34, 98-110.

Vincent. D. G., T. Q. Carney, J. H. Homan, and R. Fulton, 1981: Mesoscale weather patterns during April 10-11, 1979 severe weather outbreak in the southwestern U.S.A. Proc. IAMAP Symposium, Hamburg, 11-16.

_____, and _____, 1982: Meso-synoptic scale circulation patterns during severe weather outbreak of April 10-11, 1979. Preprints, Twelfth Conf. Severe Local Storms, San Antonio, 556-559.

_____, and T. W. Schlatter, 1979: Evidence of convection as a source of synoptic-scale kinetic energy. Tellus, 31, 493-504.

Ward, J. H, and P. J, Smith, 1976: A kinetic energy budget over North America during a period of short synoptic wave development. Mon. Wea. Rev., __, 836-848.

| 1. REPORT NO. NASA CR-3820 | 2. GOVERNMENT ACCESSION NO. | 3. RECIPIENT'S CATALOG NO. |
|---|---|---|
| 4. TITLE AND SUBTITLE  A Kinetic Energy Study of the Meso β-Scale Storm Environment During AVE-SESAME V (20-21 May 1979) | | 5. REPORT DATE  August 1984 |
| | | 6. PERFORMING ORGANIZATION CODE |
| 7. AUTHOR(S)  Matthew F. Printy and Henry E. Fuelberg | | 8. PERFORMING ORGANIZATION REPORT # |
| 9. PERFORMING ORGANIZATION NAME AND ADDRESS  Department of Earth and Atmospheric Sciences  Saint Louis University  Saint Louis, Missouri  63103 | | 10. WORK UNIT NO.  M-442 |
| | | 11. CONTRACT OR GRANT NO.  NAS8-33370 |
| 12. SPONSORING AGENCY NAME AND ADDRESS  National Aeronautics and Space Administration  Washington, DC  20546 | | 13. TYPE OF REPORT & PERIOD COVERED  Contractor Report |
| | | 14. SPONSORING AGENCY CODE |

15. SUPPLEMENTARY NOTES

Marshall Space Flight Center, Systems Dynamics Laboratory
Technical Monitor:  Dr. Gregory S. Wilson, ED44
Interim Report

16. ABSTRACT

An area of intense thunderstorms occurred over the special mesonetwork in central Oklahoma that was operated during the fifth AVE-SESAME period of 1979 (20-21 May). These meso 6-scale data are used to conduct a kinetic energy analysis of the near storm environment.

Horizontal winds in the 400-150 mb layer strengthen rapidly north of the developing convection.  Peak values then decrease such that the maximum disappears 6 h later. Southeast of the storms, wind speeds above 300 mb decrease nearly 50% during the 3 h period of most intense thunderstorm activity.  On the other hand, conditions near 400 mb are quite different since winds nearly double as the convection forms.  When the convection dissipates, wind (energy) patterns return to pre-storm conditions.

The mesoscale storm environment of AVE-SESAME V is characterized by large values of cross-contour generation of kinetic energy, transfers of energy to non-resolvable scales of motion (negative dissipation), and horizontal flux divergence.  These processes are maximized within the upper troposphere and are greatest during times of strongest convection.  Energy analyses also are obtained from the routine National Weather Service rawinsonde network.  A comparison of results from the same analysis region, but derived from the two different resolutions, reveals many common features.

Spatial maps of energy budget terms show that patterns agree closely with observed weather features.  The southeast area of the network is examined in detail to determine causes for vertical wind variations.  Motions not detected by the input data appear to play an important role in the energy balance of some layers.

| 17. KEY WORDS  Kinetic energy budgets  Mesoscale convection  Scale interaction  AVE-SESAME V | 18. DISTRIBUTION STATEMENT  Unclassified - Unlimited  Subject Category 47 |
|---|---|
| 19. SECURITY CLASSIF. (of this report)  Unclassified | 20. SECURITY CLASSIF. (of this page)  Unclassified |

| 19. SECURITY CLASSIF. (of this report) | 20. SECURITY CLASSIF. (of this page) | 21. NO. OF PAGES | 22. PRICE |
|---|---|---|---|
| Unclassified | Unclassified | 110 | A06 |

1